Mechanical Systems and Signal Processing 232 (2025) 112702

Contents lists available at ScienceDirect

Mechanical Systems and Signal Processing

journal homepage: www.elsevier.com/locate/ymssp

Full Length Article

A novel data-driven K-SVD transferrable baseline method for multi-damage identification for composite fuselage panels

Haomiao Fang *, Zahra Sharif Khodaei, Ferri M.H. Aliabadi

Department of Aeronautics, Imperial College London, South Kensington Campus, Exhibition Road, SW7 2AZ London, UK

ARTICLE INFO

Keywords:
Transferrable baseline
K-SVD
Shapelets
Scalable
Reliability-based threshold
Curved fuselage panels

ABSTRACT

This paper presents a novel, scalable, data-driven, and transferrable baseline framework for damage detection and localization in large, complex composite structures operating under in-service conditions, such as varying temperatures. The proposed approach addresses a key challenge in the adoption of ultrasonic guided wave Structural Health Monitoring (SHM) for damage detection in large structures: the need to collect baseline measurements.

The proposed framework detects damage in composite fuselage panels by creating a dictionary of pristine data from simpler structural components, i.e. flat composite coupon panels and mono-stringer elements. By utilizing shapelets generated at these lower structural levels, the methodology can be extended to more complex geometries, accommodating variations in temperature, material properties, sensor configurations, and specimen sizes, making it suitable for structures in service. The framework is built around the K-SVD algorithm, which efficiently captures the most representative shapelets while significantly reducing computational time. The reliability and accuracy of the algorithm are validated using pristine coupon data to minimize false alarms, and the approach is then scaled to address more complex curved fuselage panels. Furthermore, the framework incorporates a reliability-based threshold into the K-SVD algorithm for the first time, establishing a detectability threshold for this transferrable baseline method and enabling both damage detection and severity assessment. The effectiveness and robustness of the methodology are demonstrated experimentally using data from large 5-meter curved fuselage panels subjected to varying temperatures and multiple damage scenarios. The results show a true positive rate of 0.951 and a false negative rate of 0.944 for damage detection in the curved fuselage panels within a temperature range of 25°C to 50°C.

1. Introduction

Structural Health Monitoring (SHM) has emerged as a novel alternative to non-destructive testing (NDT), with a wide application in aeronautical engineering to ensure the structural integrity and operational safety of aircraft [1–4]. By providing remote monitoring, early damage detection and enabling predictive maintenance, SHM systems significantly enhance the operational capabilities and cost-effectiveness of aerospace structures [5–7]. Guided wave based SHM (GWSHM) is one of the promising and powerful SHM techniques for barely visible impact damage (BVID) detection in aircraft structures, due to its advantages of large inspection coverage within

* Corresponding author.
E-mail addresses: haomiao.fang22@imperial.ac.uk (H. Fang), z.sharif-khodaei@imperial.ac.uk (Z.S. Khodaei), m.h.aliabadi@imperial.ac.uk (F.M.H. Aliabadi).

https://doi.org/10.1016/j.ymssp.2025.112702
Received 26 November 2024; Received in revised form 2 April 2025; Accepted 3 April 2025
Available online 17 April 2025
0888-3270/Crown Copyright © 2025 Published by Elsevier Ltd. This is an open access article under the CC BY license (http://creativecommons.org/licenses/by/4.0/).

complex geometries, high damage sensitivity and detailed damage characterization [2,8–10]. This technique is mainly comprised of permanently installed piezoelectric (PZT) transducers, guided wave generation and capture, sophisticated signal processing and damage identification algorithms [11,12].In monitoring composite aircraft structures, GWSHM faces several specific challenges in complex geometries such as curvature and varying thicknesses, mode conversion and dispersion [13], sensor placement and integration [14]. It is also well-known that guided waves are severely affected by the changes in environmental and operational conditions (EOCs), especially due to temperature variations. To address this problem, temperature compensation has been implemented to conventional baseline damage detection approach to eliminate the phase delay and amplitude changes [15]. Contrast to the baseline approach that relies on comparing current measured data to the baseline, baseline-free approach allows for the identification and assessment of damage within a structure without the need for baseline data from an undamaged state. Related leading baseline-free techniques include time reversal imaging [16,17], reciprocity [18], instantaneous approach, etc.

Despite their potential benefits, the existing baseline-free techniques have limited application to real aircraft damage detection. The main reason is that the complexity of Lamb wave propagation increases with the complexity of the structure. However, for baseline-free techniques, the wave propagation is only approximated by the limited physics-based hypotheses [17,19–21]. Accurately modelling and interpreting the wave propagation without a baseline becomes significantly more difficult. Another limitation is the high sensitivity to environmental conditions [8], such as temperature, humidity, and loading fields. These variations can affect the propagation characteristics of the waves and complicate the interpretation of results. Nevertheless, few works have been carried out to validate the robustness of the proposed baseline-free techniques under varying EOCs or increasing geometrical complexities. Typically for conventional baseline methods, an empirical threshold is set to distinguish the damaged state and avoid false alarm. A statistical threshold was proposed by Yue et al. to include EOC variability in the outlier analysis to identify anomalous data from normal data with high confidence [22]. They proposed a Mahalanobis Square Distance (MSD) to represent the degree of discordance of the damage index vector from the baseline data set. This outlier analysis was further extended by Rodrigues et al. [14] to define the detectability threshold for curved fuselage panels. The detectability threshold is generated based on a pristine database for an actual airframe component of real size and complexity. However, this reliability-based threshold is developed for the conventional baseline method and is not compatible with any existing baseline-free or transferrable baseline technique for damage detection. Without a baseline, the existence and severity of the damage is challenging to be detected despite its potential successful localisation, which leads to an increased risk of false positives (detecting defects that are not present) and false negatives (failing to detect actual defects).

Recent studies have increasingly focused on using statistical properties of guided wave signals to improve robustness against EOCs in SHM applications. Nerlikar et al. [23] proposed a physics-embedded deep learning framework that integrates multi-fidelity modeling, while Fisher et al. [24] employed denoising autoencoders to compensate for temperature-induced variations, both highlighting the role of adaptive statistical modeling. Mesnil et al. [25] introduced a self-referenced defect detection approach that exploits signal consistency for enhanced adaptability in complex structures. Additionally, Tu et al. [26] and Ahmed & Kopsaftopoulos [27] explored time-series models such as nonlinear autoregressive (NARX) and stochastic stationary models, respectively, demonstrating their effectiveness in capturing underlying statistical patterns for damage diagnosis. Notably, Nerlikar et al. [28] introduced the aggregated baseline concept, constructing an adaptive statistical reference from historical data rather than relying on fixed pristine signals, thereby significantly improving robustness to EOCs. However, the applicability of these methods to large scale complex composite structures has not been demonstrated.

Based on the above-mentioned challenges, a novel scalable data-driven K-SVD based transferrable baseline framework is proposed in this work for damage detection and localisation, which does not require prior deterministic pristine data base. The novel methodology is developed for complex composite structures such as curved fuselage panels, utilising data only from coupons (flat composite panels) and elements (mono-stringer panels) at lower structural levels. Based on the shapelets (subsequence of the signal) generated at lower and less complex levels of the building block (BB), the methodology is upscaled to more complex geometries, independent of temperature variants, material properties, sensor configurations, specimen sizes, etc. In addition, a reliability-based threshold is integrated into the proposed K-SVD based framework for the first time to define the detectability threshold for a transferrable baseline method, and to further detect the damage existence and severity.

K-SVD was originally proposed by [29] for dictionary learning and sparse coding, which was later widely applied in image enhancement, compression, and pattern recognition. However, few studies have investigated its applications in the GWSHM damage identification problem here. Regarding dictionary learning and sparse coding, the related work includes contributions by [30] who presents an adaptive dictionary learning framework for damage localization in complex structures. However, the proposed approach is still a baseline one. Further work is carried out by [31] who achieved baseline-free damage detection within four Aluminium plates. Despite the successful localisation based on full wavefield data, the proposed approach has not been applied to real aircraft structures with increasing structural complexities. Recently, an unsupervised shapelets and shift-invariant dictionary learning method have been utilised for damage identification [32]. This technique can be applied to structures with different sensor configurations and specimen sizes and has significantly improved the localisation accuracy [32]. However, a decreased detection capability and larger detection error have been found in the stiffened panel with increasing structural complexities, which becomes a constraint for its further application. Besides, the algorithm is computationally expensive and impractical for large data sets. This main problem is addressed by using K-SVD in this study. The K-SVD algorithm is employed to efficiently construct a dictionary consisting of numerous shapelets. It is demonstrated that a dictionary created with coupons and mono stringers can capture sufficient information for detecting damage in a larger, industrial-scale 5-meter curved fuselage panel. This generated dictionary effectively identifies damage within a complex structure, even under varying temperature conditions. Additionally, virtual baselines are reconstructed using sparse coding with the generated dictionary. These reconstructed baselines are then compared with the current measured signals to identify damage. A reliability-based threshold is incorporated into the proposed framework to assess both the presence and severity of damage. Compared

with the existing unsupervised shapelets algorithm [33], it is shown that the proposed K-SVD shaplets carry the most fundamental and calibrated information of healthy signals within a much shorter learning time. The study also validates the robustness of the proposed technique for the structure at different levels of geometrical complexities and under varying temperature within the range of [20:5:45]°C.

The manuscript is organized as follows. Section 2 introduces the framework of the proposed technique and details the developed methodology and algorithms. The work is presented in four steps: pre-processing, dictionary generation, signal reconstruction and damage identification. Section 3 details the steps of the dictionary generation based on the pristine data set. In Section 4, the detectability of the proposed methodology is verified based on the pristine data to avoid the false alarm. In Section 5, the robustness and effectiveness of the proposed methodology are validated based on the damage identification outcome. Section 6 introduces the damage detection and localization on complex curved fuselage panels under varying temperature, and for multiple damage scenarios.

2. Methodology

This section presents a novel transferrable baseline guided wave damage detection approach based on K-SVD online dictionary learning and sparse coding to detect and localize barely visible impact damage (BVID) on complex composite structures. By applying K-SVD algorithm (with enough iterations), the learnt shapelets can capture the most fundamental information of the Lamb wave signals from the healthy structures, as long as the waveforms in the underlying structures are of similar form. This means that the signal reconstruction is not influenced by small changes in material properties, specimen sizes, temperature fields, and sensor configurations. These learnt shapelets function as the dictionary atoms when carrying out sparse coding. In sparse coding, the current measured signal is described and reconstructed by sparse linear combinations of these atoms [29]. The reconstructed signal is 'healthy' and serves as the virtual baseline for the inspected structure since the trained shapelets (atoms) are all learnt from signals of the healthy structures. The overview of the proposed methodology is illustrated in Fig. 1.

As illustrated in Fig. 1, the proposed methodology is organized into three main modules. First, in Module A: Dictionary Generation, the training dataset consists of a substantial number of pristine signals used to generate the dictionary. This dictionary is composed of

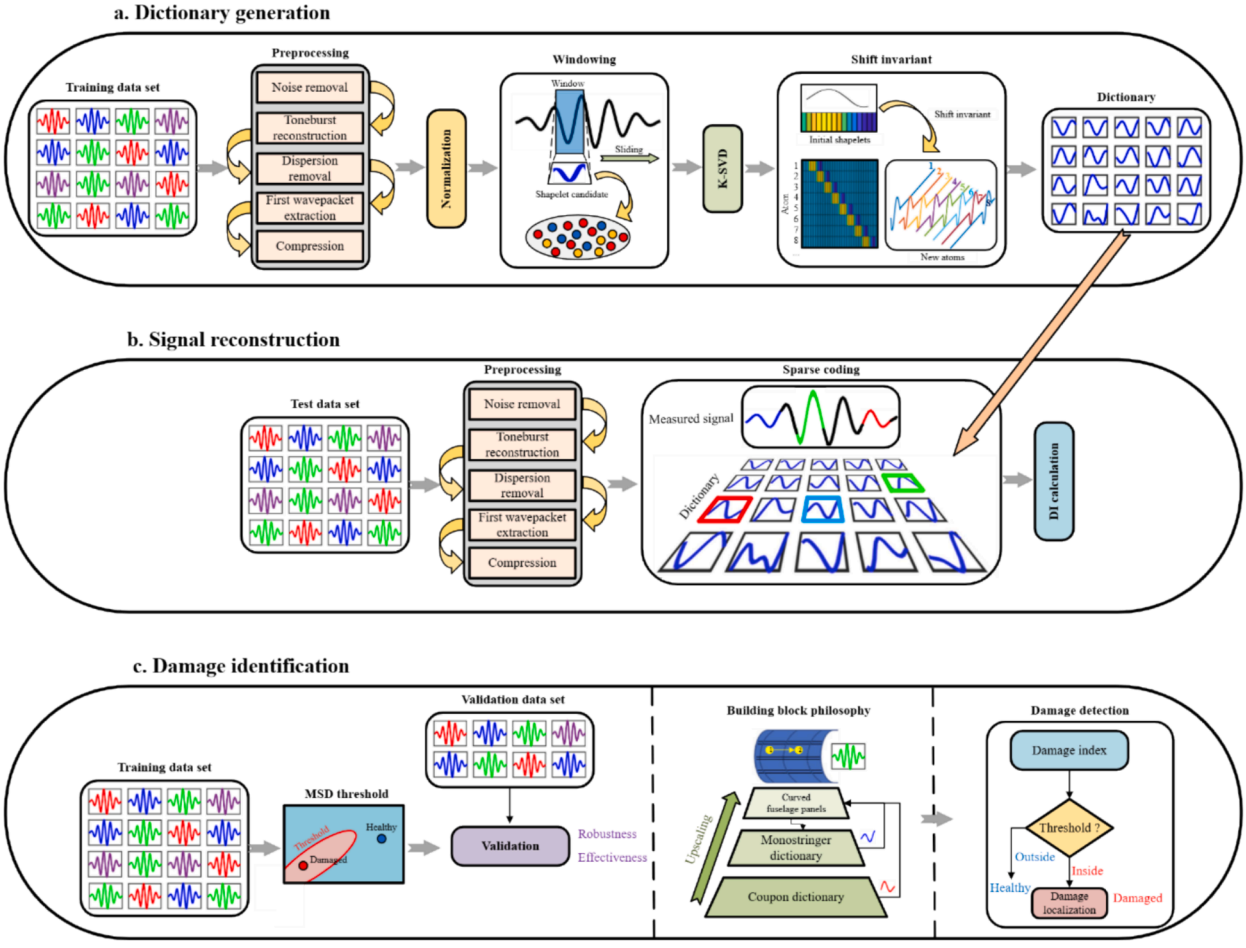


Fig. 1. Overview of the proposed K-SVD based transferrable baseline damage identification framework.

iteratively learned shapelets that capture the most fundamental and calibrated characteristics of healthy signals. The main novelty of the proposed framework is that the dictionary generation is done based on data from simple structures tested in the laboratory (coupon and mono-stringer) only, and it is transferred to a more complex structures such as a large fuselage panel. In other words, the baseline reconstruction follows a building block approach and is transferred to higher levels, without requiring any additional training. In this work, the proposed methodology is developed and validated for a large composite fuselage panel, which requires the dictionary to be generated based on the lower levels of the BB, i.e. coupon and mono-stringer panels.

Based on this dictionary, Module B: Sparse Coding applies sparse coding techniques to reconstruct test signals. Through this process, Damage Index (DI) values are calculated for each transducer path, which are then employed for damage detection and localization in Module C.

Preprocessing steps are performed in both Modules *A* and *B* to optimize signal reconstruction. These steps include noise removal, toneburst reconstruction, dispersion removal, first wavepacket extraction, and signal compression, as shown in Fig. 1.

2.1. Preprocessing

To remove the noise and enhance the signal-to-noise ratio (SNR), averaging technique is applied in this study where 10 consecutive measurements are acquired under the same conditions. By averaging these recorded signals, the influence of random noise can be eliminated.

The linear chirp signal within the range of 10 kHz − 600 kHz is generated as the excitation signal. The acquired response can then be reconstructed to the 5-cycle Hanning windowed toneburst signal at any central frequency between 10 and 600 kHz, which saves much time and data storage, and enables transferable baseline reconstruction for various guided waves modes.

To eliminate the wave dispersion and separate the wave packets from other modes [34], a dispersion removal technique [35] has been adopted. This technique works mainly based on the concept that the dispersion can be removed by mapping the original dispersion relation into a new linear one. The procedure has been summarized in Fig. 2. Here, the sensor-received signal can be denoted as $g(t)$. Firstly, fast Fourier transform (FFT) is applied to obtain the frequency spectrum $G(\omega)$, where $G(k) = G(\omega)$ since the wavenumber k is a function of ω [36]. Secondly, the linear wave relation based on the Taylor expansion is obtained. Then, the modified frequency spectrum $\widetilde{G}(\omega)$ can be calculated through interpolation. Subsequently, a signal $\tilde{g}(t)$ with the dispersion removed can be obtained. Refer to [35] for more details of dispersion removal algorithm.

Additionally, the first wavepacket extraction and normalization (which rescales the signal amplitude within [-1,1]) are implemented to mitigate phase and amplitude variations induced by temperature changes.

2.2. K-SVD

Shapelets are time series subsequences which are maximally representative of a class [37]. Unsupervised shapelets algorithm has been implemented to cluster time series and generate the representative shapelets [33]. However, this method mainly has two limitations. Firstly, it requires too much power and is time-consuming for large data sets [38]. Secondly, the number of learnt shapelets cannot be flexibly controlled. To address these challenges, a novel K-SVD algorithm has been employed to generate shapelets in this work. An excessive or insufficient number of shapelets can lead to redundancy or a lack of critical information in the dictionary. The K-SVD algorithm, originally proposed by [29] for designing overcomplete dictionaries for sparse representation, is particularly well-suited for this problem. This approach allows for a more controlled and efficient generation of shapelets, improving both the quality and the relevance of the resulting dictionary.

Algorithm 2 (refer to Appendix A) outlines the procedure for shapelet generation using K-SVD. Assume $y \in \mathscr{R}^{L\times N}$ represents the training matrix that includes N shapelet candidates of length L. $D \in \mathscr{R}^{L\times K}$ is the dictionary that includes K shapelets of length L. The initial dictionary $D^{(0)} \in \mathscr{R}^{L\times K}$ is composed of K numbers of ℓ^2 normalized columns. $x \in \mathscr{R}^{K\times N}$ represents the sparse representation matrix. Therefore, the problem of searching the best possible dictionary can be expressed by equation (1) [39]:

$$\min_{D,\,x}\left\{\|y - Dx\|_F^2\right\} \quad \text{subject to}\ \forall i,\ \|x_i\|_0 \le T_0 \tag{1}$$

Where $\|x_i\|_0$ is the ℓ^0 norm, which represents the number of non-zero elements in x_i. T_0 is the sparsity constraint that needs to be small enough.

For a fixed dictionary D, the sparse representation of each shapelet candidate y_i (each column in y) is obtained by solving the following optimization problem:

$$x_i = \operatorname{argmin}_x\left\{\|y_i - Dx_i\|_2^2\right\} \quad \text{subject to}\ \forall i,\ \|x_i\|_0 \le T_0 \tag{2}$$

Once the sparse representations are computed, the dictionary is updated iteratively. The update process is performed atom by atom to refine the dictionary while maintaining the sparsity of x. For each dictionary atom d_k, with the corresponding row in x denoted as x_T^k,



Fig. 2. Schematic sketch of the dispersion removal technique.

the error matrix E_k is computed as:

$$E_k = y - \sum_{j \neq k} d_j x_T^j \tag{3}$$

Where E_k represents the residual when excluding the contribution of d_k. The objective is then to update d_k and x_T^k by minimizing the Frobenius norm of the residual. The process can be expressed by:

$$P = \| \left(y - \sum_{j \neq k} d_j x_T^j \right) - d_k x_T^k \|_F^2 \tag{4}$$

$$P = \| E_k - d_k x_T^k \|_F^2 \tag{5}$$

Where P represents the penalty term, of which the minimization problem can be efficiently solved using Singular Value Decomposition (SVD). Consequently, the method alternates between the sparse coding step and the dictionary update step until convergence is achieved.

2.3. Damage detection

For the transducer path i, the damage index, denoted by DI_i, can be defined as the cross-correlation coefficient of the first wave packet of the test signal S_i and its reconstructed one $\widetilde{S}_i$ based on sparse coding:

$$DI_i = 1 - corr\left(S_i, \widetilde{S}_i \right) \tag{6}$$

Then, the damage index vector for the section including N transducer paths, denoted by DI_s, can be defined by equation (7):

$$DI_s = [\mu, \sigma],\ \mu = \frac{\sum_{i=1}^{N} DI_i}{N},\ \sigma = \sqrt{\frac{\sum_{i=1}^{N} (DI_i - \mu)^2}{N-1}} \tag{7}$$

To distinguish between healthy and damaged states, a reliable threshold needs to be defined. The outlier analysis combined with the building block philosophy is utilized in this paper [40]. For a damage index vector DI_s for the section, the discordance of this vector from the reference (pristine state) data set can be described by the Mahalanobis Square distance [41,42] (MSD). The MSD of DI_s to the reference data set $DI_s{}^0$ is given by equation (8):

$$MSD = \sqrt{\left(DI_s - \overline{DI_{s_T}^0} \right)^T [S]^{-1} \left(DI_s - \overline{DI_{s_T}^0} \right)} \tag{8}$$

Where $\overline{DI_{s_T}^0}$ and S are the mean vector and covariance of the reference data set, respectively.

Reliability assessment adapted from [43] has been used to evaluate the detection performance. The accuracy of the applied outlier analysis is defined by equation (9):

$$Accuracy = \frac{TP + TN}{TP + TN + FP + FN} \tag{9}$$

Where TP, TN, FP, FN are defined in Table 1.

2.4. Damage localization

The Reconstruction Algorithm for Probabilistic Inspection of Damage [22,44] (RAPID) is implemented for damage localization, which leverages probabilistic and statistical techniques to robustly inspect and assess damage in structures. In this method, the likelihood of damage presence, location, and severity are represented based on the fusion of signals rendered by several actuator-sensor elliptical paths. For RAPID algorithm, the imaging field $I_{RAPID}(x, y)$ is formulated by equations (10) (11) (12):

Table 1
Detection outcomes.

Predicted state	Ture state $d = 0$	$d = 1$
$\widehat{d} = 0$	True negative (TN)	False negative (FN)
$\widehat{d} = 1$	False positive (FP)	True positive (TP)

$$I_{RAPID}(x,y) = \sum_{i=1}^{n} DI_i \bullet R_j(x,y) \tag{10}$$

$$R_j(x,y) = \begin{cases} f_j(x,y), @f_j(x,y) < \beta \\ \beta, @f_j(x,y) \geq \beta \end{cases} \tag{11}$$

$$f_j(x,y) = \frac{\sqrt{(x-x_a)^2 + (y-y_a)^2} + \sqrt{(x-x_r)^2 + (y-y_r)^2}}{\sqrt{(x_r-x_a)^2 + (y_r-y_a)^2}} \tag{12}$$

Where *a, r* corresponds to the actuator and sensor of the transducer path *i*. β is set as 1.05 to adjust the coverage of the transducer path.

2.5. Theoretical explanation for pseudocode

2.5.1. Windowing algorithm

The windowing algorithm (run in MATLAB 2022) has been applied to extract segments from pristine signals and generate shapelet candidates [32]. As is illustrated in Fig. 3, a window of length L is constructed and slides along the time series signal. For a time-series of length L_0, (L_0-L + 1) shapelets of length L can be generated. Algorithm 1 (refer to Appendix A) outlines the procedure for shapelet candidate generation.

2.5.2. K-SVD

Sparse coding is applied to compute the corresponding sparse representation vector x_i for each shapelet candidates y_i when the dictionary matrix is fixed (line 5–10). Algorithm 3 (refer to Appendix A) explains the details of Orthogonal Matching Pursuit (OMP) algorithm [45]. Line 11–19 is the dictionary update stage. Both sparse representation matrix x and dictionary D are fixed except for only one column in D to be updated. Consequently, we only need to consider $D(:,k)$ (the kth column in D) and the corresponding $x(k,:)$ (the kth row in x). Inside the dictionary update loop, line 12 looks for all nonzero entries in $x(k,:)$. Line 13 defines E_k as the relevant error matrix. Then, E_k and $x(k,:)$ are restricted to those columns where $x(k,:)$ is nonzero (line 14–15). Line 16 performs Singular Value Decomposition (SVD). Then, the dictionary column $D(:,k)$ and the corresponding sparse vector are updated in lines 17–18. Repeat the procedure until the convergence is reached. Refer to [29] for more details of the K-SVD algorithm.

2.5.3. Shift invariant

The obtained shapelet dictionary from K-SVD algorithm cannot be directly used for sparse coding since the length of the shapelet is shorter than test signals. To solve this problem, the shapelet dictionary is re-arranged in a shift-invariant form based on Algorithm 4

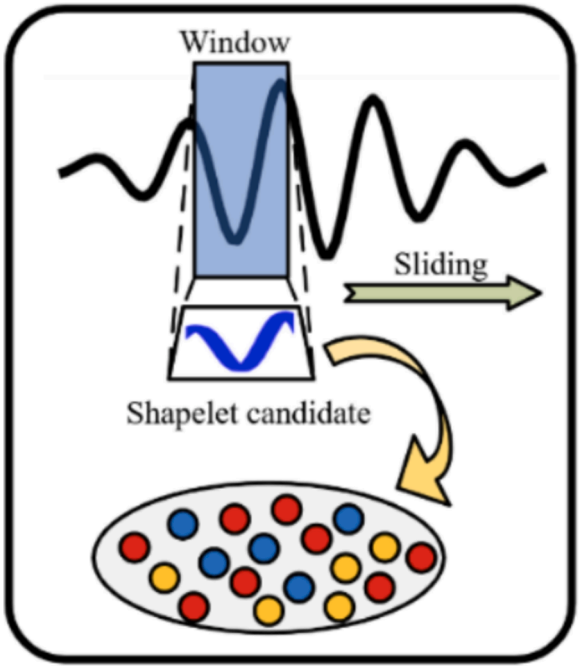


Fig. 3. Illustration of the windowing algorithm.

(refer to Appendix A) run in MATLAB 2022. For shapelets of length L and test signals of length L_2 ($L_2 \gg L$), (L_2-$L+1$) new atoms can be generated with the length L_2. For each atom, the initial shapelet (of length L) shifts from the 1st up to the (L_2-$L+1$) th position, with other entries zero, which is depicted in Fig. 4. Consequently, for a series of atoms based on the same shapelet, they share the same shapelet information but different time delays (different phases).

3. Dictionary generation

3.1. Training data set

To ensure the learnt shapelets capture the most fundamental information of healthy signals, the pristine training data set [14,15,46,47] needs to be large and diverse enough. In this work, a significant number of signals for the structures with different material properties, specimen sizes, sensor configurations and temperature variation are included in the training data set, which is illustrated in Table 2 (refer to Appendix B for a complete table). The shapelets generated at the lower coupon and element level are then upscaled to the sub-component level for further analysis and validation.

In Table 2, the total number of signals is calculated as the number of panels × the number of signals per panel, where the number of signals per panel is decided by the sensor network size. For the n-sensor network, the number of signals per panel should be $n \times (n-1)$. Consequently, in this work, 3040 healthy signals of coupons and 280 healthy signals of mono-stringer panels are included. All signals are reconstructed to the 5-cycle Hanning windowed toneburst signal under the frequency of 50 kHz.

3.2. K-SVD dictionary learning

3.2.1. Parameter setting

For simplification and to boost the speed of K-SVD dictionary learning process, the signal (first wavepacket) will be compressed at the ratio of 1:100. In this work, the discrete signal length and that of the first wavepacket are 30,000 and 8,000, respectively. Subsequently, the length of the compressed first wavepacket was down to 80.

After compression, the normalization is applied and the signal is rescaled within the range [-1,1]. This could ensure the regularization parameter in the following sparse coding stage to be at the same level when dealing with different damage cases. (Note that for K-SVD stage, the regularization parameter is set to be one.).

The length of shapelet candidates is set to be one fifth of the first wavepacket. For a given signal with 80 datapoints, the length of shapelet candidates is 16, which is an empirical number that is suitable for shapelet generation.

At K-SVD stage, the numbers of learnt shapelets are set to be 30 and 20 for coupons and mono-stringer signals, respectively. The overall empirical parameters are given in Table 3.

3.2.2. Outcome

Based on windowing algorithm in Section 2.5.1, for the signal of length 80 and shapelet candidate of length 16, 65 shapelet candidates were generated per signal. Subsequently, the total number of shapelet candidates is 65 × 3040, 65 × 280 for coupon and mono-stringer panels, respectively. Recall that the objective function is:

$$\min_{D,\,x}\left\{\|y - Dx\|_F^2\right\} \quad \text{subject to } \forall i,\ \|x_i\|_0 \le T_0 \tag{13}$$

In this study, two types of shapelet dictionary (coupon dictionary and mono-stringer dictionary) have been generated separately based

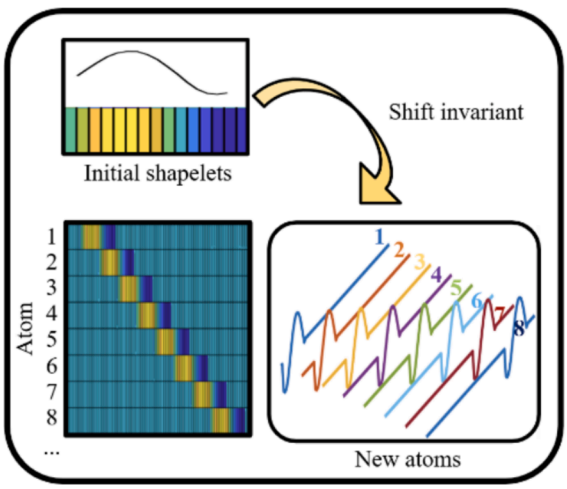


Fig. 4. Illustration of the shift invariant technique.

Table 2
Pristine data set distribution.

No	Structure items	Dimensions ($mm \times mm$)	Thickness (mm)	Material	Number of plies	Sensor network size	Temperature conditions (°C)	Total number of signals
1	Coupon	450 × 450	2	IM7-8552	16	8	[-20:5:50]	15 × 56
2	Coupon	400 × 400	2.2	T800-M21S	12	9	20	1 × 72
3	Coupon	300 × 225	2.2	T800-M21S	12	8	[-50:5:70]	25 × 56
4	Coupon	300 × 225	2.79	PEEK/HTA-40	9	8	[-15:5:45]	11 × 56
5	Coupon	500 × 500	1.8	T300	9	8	20	1 × 56
6	Coupon	500 × 500	–	–	–	8	–	1 × 56
7	Mono-stringer	500 × 250	2.2	T800-M21S	12	8	–	1 × 56
8	Mono-stringer	500 × 250	2.2	T800-M21S	12	8	[20:5:35]	4 × 56

Table 3
Parameters for K-SVD dictionary learning.

Compression ratio	Length of signal after compression	Length of first wavepacket	Length of shapelet candidates
1:100	300	80	16
Number of learnt shapelets	Sparsity constraint	Regularization	Iterations
30/20	5	1	1000

on their respective pristine data set using K-SVD algorithm. For the generation of coupon dictionary, the dimension of y should be 16 × 197,600. The dictionary D is set to be 16 × 30, which is an overcomplete dictionary since 197,600 ≫ 30. By the same token, the dimension of y and D is 16 × 18,200 and 16 × 20 for the mono-stringer dictionary, respectively. When applying K-SVD, both are shown to have a rapid convergence, which is shown in Fig. 5. In addition, the generated dictionaries are shown in Fig. 6.

4. Pristine signal verification

In this section, the reliability of the reconstructed signals is verified at the coupon level. The reconstructed baselines are compared with the original signals to ensure that there are no false alarms rates. In addition, the tolerance of the reconstructed baseline is used to propose a reliability-based threshold for damage detection to minimize false alarm rates. In addition, since the baseline signal is reconstructed, it should be demonstrated that in case of a damage current state, the reconstructed baseline does not fully match the current signal, and hence can be reliably used for damage detection. For baseline reconstruction, the sparse coding technique is implemented here.

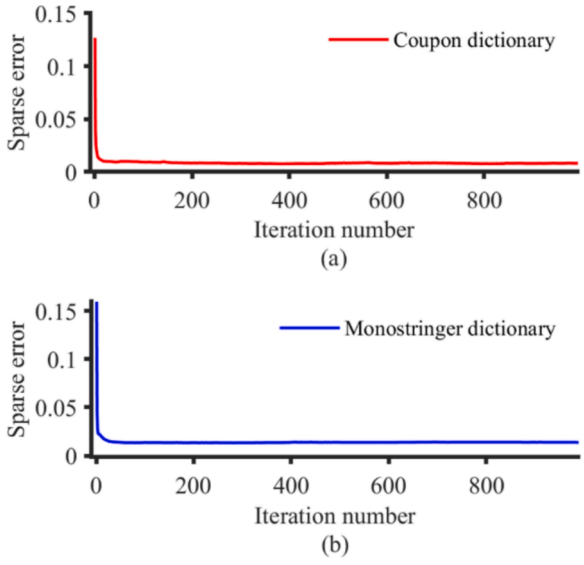


Fig. 5. Sparse error of (a) coupon dictionary generation and (b) mono-stringer dictionary generation.

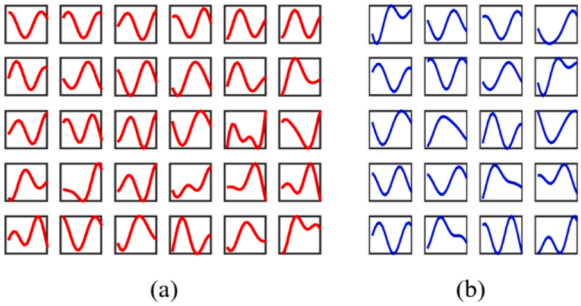


Fig. 6. K-SVD shapelet dictionaries of (a) coupon and (b) mono-stringer panels.

4.1. Sparse coding

At the stage of signal reconstruction, sparse coding is implemented to dynamically reconstruct the test signal as a linear combination of the shift dictionary atoms, which is depicted in Fig. 7. The sparse coding process can be formulated by equation (14):

$$\min_x \left\{ \|y - Dx\|_F^2 + \lambda \|x\|_1 \right\} \tag{14}$$

Where y, D, x, λ represent test signal matrix, shift dictionary, sparse representation, and regularization parameter, respectively. The regularization parameter λ controls the strength of the penalty, as well as sparse accuracy.

Unlike in equation (1), the entire sparse coding process is performed with a fixed dictionary D. In this study, LASSO regression (Least Absolute Shrinkage and Selection Operator) is used for sparse coding. In this regression, a smaller λ value applies less regularization, while a larger value applies more regularization. For coupon panels, the empirical regularization parameter (λ) value is set to be 10^{-2}. For elements and sub-components, λ is set to be 10^{-6}. As an example, Fig. 8 presents the reconstruction results for both healthy and damaged signals in coupon panels. These pre-defined empirical parameters work effectively across most panels, even with variations in size, material properties, and sensor configurations. Additionally, they help prevent overfitting.

As shown in Fig. 8, the reconstruction performance for the damaged signal in Fig. 8 (b) deteriorates significantly compared to the healthy signal in Fig. 8 (a) when using a fixed dictionary D and regularization parameter. By analyzing the reconstruction deviation—the difference between the test signal (solid blue line) and its reconstructed baseline (dashed red line), damaged signals can be effectively distinguished from the entire set of test signals.

4.2. Detectability threshold for coupon panels

As indicated in Fig. 8 (a), the residual between the test signal and its reconstructed baseline naturally persists in the reconstruction, which could potentially lead to false alarms in healthy structures. To avoid this false alarm, the detectability threshold curve is computed based on the training data set in Table 4 (refer to Appendix B for a complete table) to distinguish the damaged states from the healthy ones. The threshold value is defined using chi-squared distribution for the pristine training data set's MSD in Section 2.3. The degree of the chi-squared distribution is set to be 2, and the critical threshold value for MSD is given as 5.9915. The degree 2 is derived from the underlying statistical model, where the MSD follows a chi-squared distribution with two independent components, σ and μ. The threshold 5.9915 corresponds to the 95 % percentile of the chi-squared distribution with the degree of 2, which represents that 95

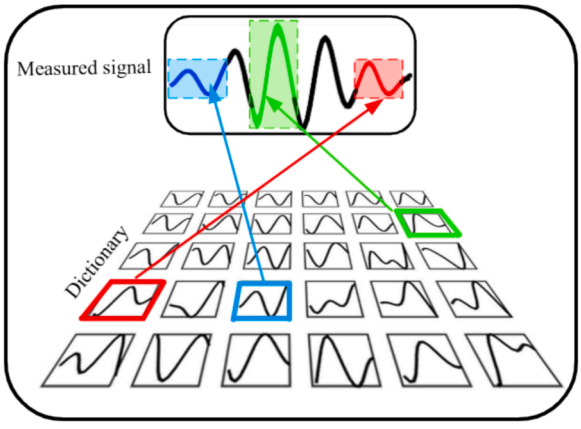


Fig. 7. Illustration of the sparse coding.

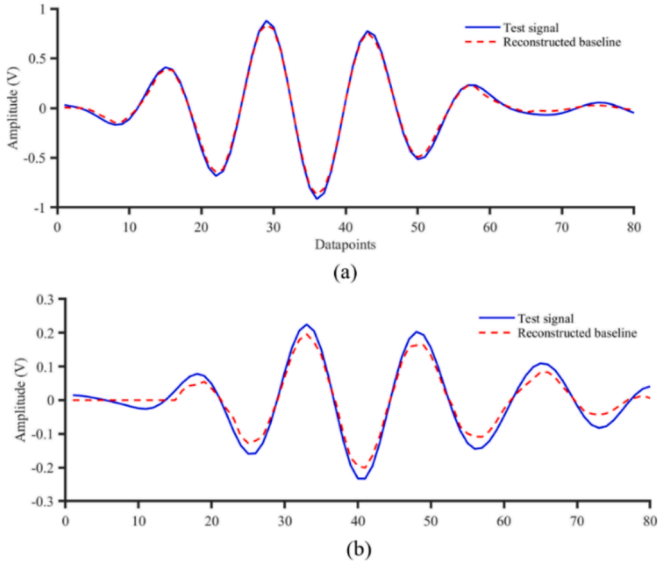


Fig. 8. Reconstruction performance of (a) the undamaged signal and (b) the damaged signal.

Table 4
Training data set distribution.

No	Structure items	Dimensions (*mm* × *mm*)	Thickness (*mm*)	Material	Number of plies	Sensor network size	Temperature conditions (°C)	Total number of signals
1	Coupon	450 × 450	2	IM7-8552	16	8	[40:5:45]	2 × 56
2	Coupon	300 × 225	2.2	T800-M21S	12	8	[-50:5:70]	25 × 56

% of MSD values fall within this threshold. This threshold effectively balances false alarms and detection sensitivity. Lower values would increase false positives by misclassifying the pristine case as damage, while higher values would reduce sensitivity, leading to undetected damage. The trained threshold curve for coupon panels is demonstrated in Fig. 9. The pristine signals of several healthy coupons are utilized for signal reconstruction based on the proposed methodology. Further evaluation of the signals for damage detection demonstrates that all pristine scenarios fall inside the set threshold, as illustrated in Fig. 10, which highlights the reliability of the baseline reconstruction and minimizing the false alarm rate.

4.3. Baseline signal verification

The overall detection outcome for coupon panels has been illustrated in Fig. 10, where all the damaged scenarios can be

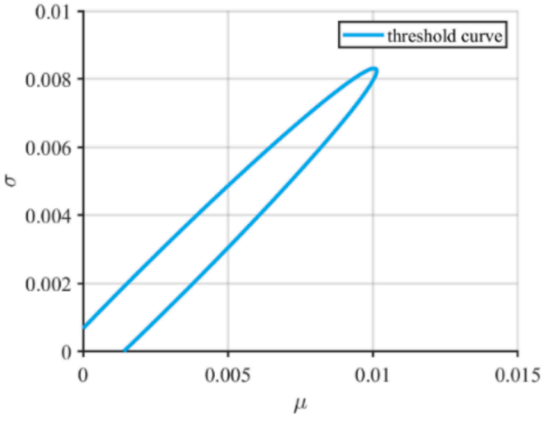


Fig. 9. MSD threshold curve of flat coupon panels.

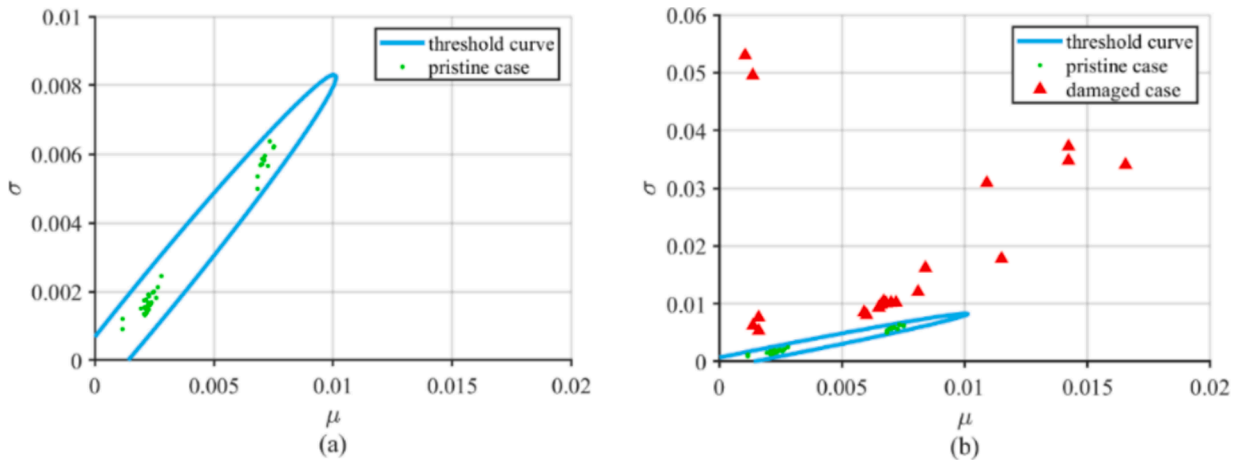


Fig. 10. Damage detection outcome for coupon level of (a) pristine cases, (b) overall cases.

distinguished well from the pristine ones. This validates the baseline reconstruction accuracy corresponding to pristine state. The *TPR*, *FAR*, *Accuracy* can be calculated by equations (15) (16) (17):

$$TPR = \frac{TP}{TP + FN} = 1 \tag{15}$$

$$FAR = \frac{FP}{TN + FP} = 1 \tag{16}$$

$$Accuracy = \frac{TP + TN}{TP + TN + FP + FN} = 1 \tag{17}$$

Consequently, the reliability of the proposed data-driven K-SVD based framework has been verified at the lower coupon level and would further be upscaled to the higher sub-component level, which hence reduces the number of tests required for the large and complex structures.

5. Validation and verification of the proposed methodology

In this section, the robustness and effectiveness of the proposed methodology is validated based on the damage identification outcome, which ensures that the damage can be detected and localized.

5.1. Damage detection under varying temperature

Damage detection under varying temperatures is used to validate the robustness of the proposed transferable baseline reconstruction methodology. This case study examines the detection of Barely Visible Impact Damage (BVID) across a temperature range

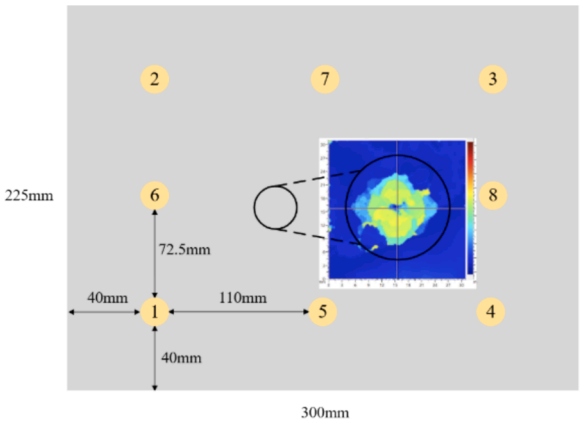


Fig. 11. A M21-T800S coupon panel impacted with the C-scan results of the damage.

from 20 °C to 45 °C in 5 °C increments. Fig. 11 illustrates the M21-T800S coupon panel, measuring 300mm × 225mm × 2.2*mm*, with a stacking layer sequence of $[\pm 45/0_2/90/0]_2$. Eight DuraAct sensors are mounted on the panel surface. BVID is introduced through a 20 J drop-weight impact. Using the K-SVD dictionary learning approach, the resulting damage detection and localization outcomes are shown in in Fig. 12 and Fig. 13, with the black circle indicating predicted damage and the yellow triangle showing actual damage. As shown, damage is effectively detected and localized at all temperatures.

Additionally, the inherent discrepancy between the predicted and actual damage is found in Fig. 13. This is because the RAPID technique predominantly focuses on the direct path between transducer pairs and relies on a dense sensor network for accurate localization. Furthermore, for the pure RAPID method as guided wave propagates, the scattering and reflections at the boundary as well as their attenuation and dispersive nature lead to the degradation of guided wave quality. This degradation reduces the temporal resolution at later time instances, further impacting damage detection accuracy [40]. Refer to Appendix E for the refined fusion PDI localization results.

5.2. Dual damages on the stiffened panel

This investigation involves detecting two separate damage sites on a stiffened panel (manufactured as part of the SHERLOC CleanSky2 project) equipped with 12 DuraAct sensors [19]. The damage was introduced by drop-weight impacts of 20 J and 35 J, respectively. Fig. 14 (a) shows the M21-T800S coupon panel, which measures 1624mm × 904mm × 2.2*mm*, with a stacking layer sequence of $[\pm 45/0_2/90/0]_2$. Following the building block approach, the detection and localization results for each element are displayed in Fig. 14 (b) and Fig. 15 (b) (c). In Fig. 15, the black circle indicates predicted damage, and the yellow triangle shows the actual damage. Both damage locations are accurately detected and localized within their respective elements, despite some artifacts along other transducer paths.

The overall probability based diagnostic imaging (PDI) in Fig. 15 (a) reveals that the detection of damage on the lower side of the stringer's foot is notably masked by the damage on the upper side at the stringer's hat. Although the impact energy on the stringer's hat is lower (20 J), the damage detection appears more prominent due to complex mode conversion and wave distortion around this area. Wave interaction with the stringers impairs reconstruction accuracy, increasing the gap between the measured and reconstructed signals. As a result, the damage index value rises, making the damage on the stringer's hat appear more severe than expected.

6. Damage identification for curved fuselage panels

6.1. Building block (BB) philosophy for transferrable baseline

A building block (BB) philosophy [40] is employed for transferrable baseline reconstruction to detect and localize damage in composite structures at increasing levels of complexity: coupon, element, and sub-component. The information flow of the BB philosophy is illustrated in Fig. 16. This approach facilitates the use of shapelets from the lower coupon and mono-stringer levels to the higher sub-component levels. Utilizing a dictionary composed of shapelets generated at these lower and less complex levels, the methodology can be scaled up to address larger and more complex geometries, while remaining independent of variations in temperature, material properties, sensor configurations, specimen sizes, and other factors.

In Level 1 and Level 2, a significant number of pristine signals for panels with different specimen sizes, material properties, sensor configurations, environmental fields etc., are utilized to generate coupon and mono-stringer dictionary, respectively. In Level 3, the above two dictionaries are integrated to analyse the stiffened panels or SHERLOC curved fuselage panels [14]. Since the guided wave signals attenuate and reflect when passing the stiffener, the effect of the stiffener needs to be specifically included in the dictionary for the sub-component. However, the skin can be represented by the vast library of coupon data which is available. Therefore, the mono-

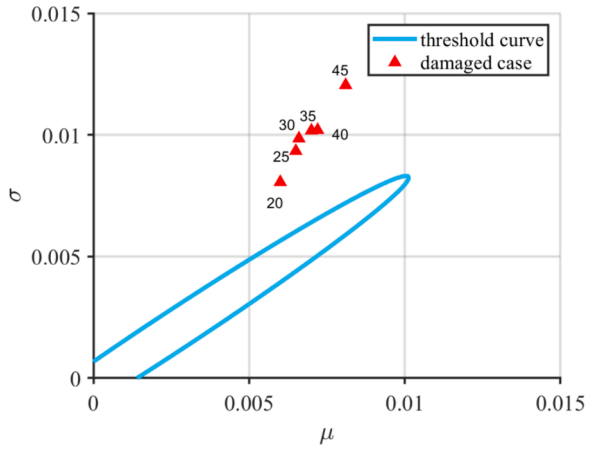


Fig. 12. Damage detection outcome of the impacts under varying temperature.

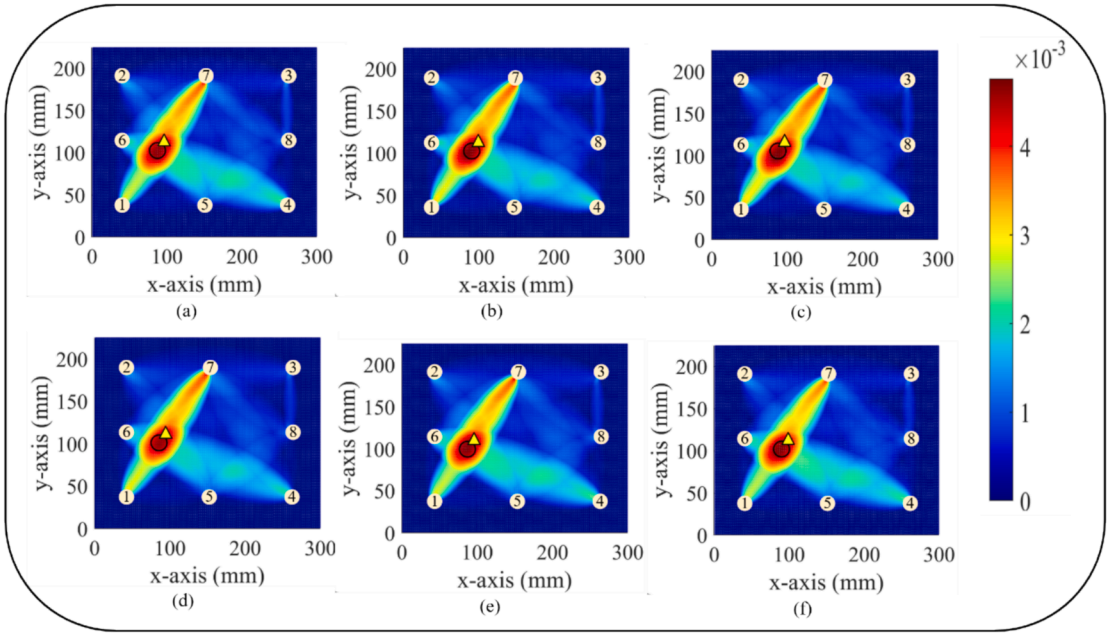


Fig. 13. Damage localization outcome of the impacts at (a) 20 °C, (b) 25 °C, (c) 30 °C, (d) 35 °C, (e) 40 °C, (f) 45 °C.

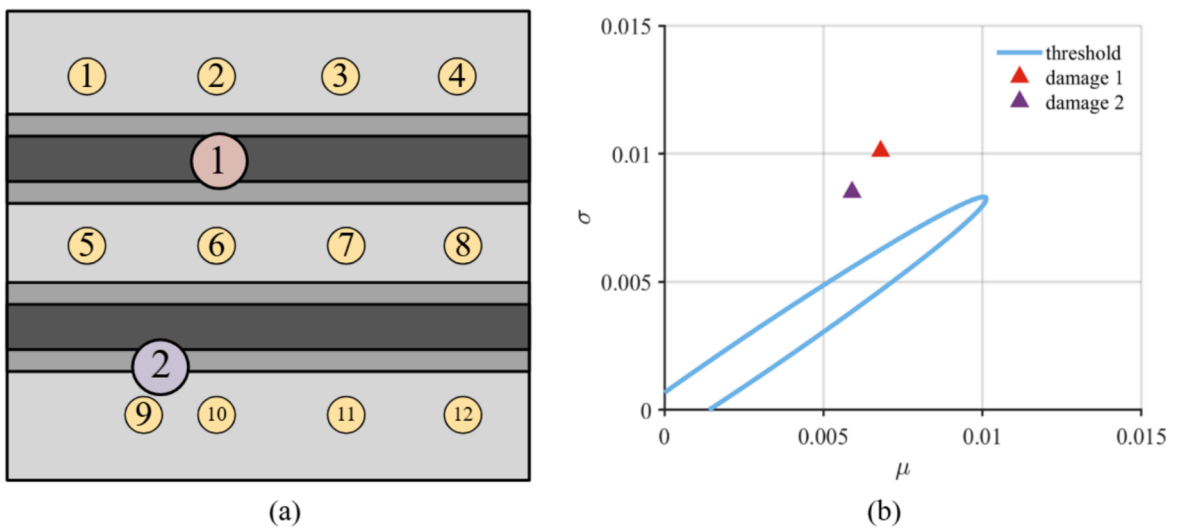


Fig. 14. (a) A M21-T800S stiffened panel for the case of the dual damage, (b) Damage detection outcome of the dual damage in the stiffened panel.

stringer dictionary is used to analyse the stiffener part of the panel while the coupon dictionary deals with other flat areas in the panel, as illustrated in Fig. 17.

6.2. *Experimental setup*

The sub-component investigated in this study is a 5-meter-long curved fuselage panel which is designed by the SI&HM group at Imperial College London and manufactured by FIDAMC within the SHERLOC CleanSky2 project. The illustration of the curved fuselage panel is given in Fig. 18 (a) (refer to Appendix C for a complete figure). The panel has a radius of 1.67 m and is constructed with 6 longitudinal CFRP stringers and 7 transverse Aluminum frames [14]. Both the skin and the stringers are manufactured using M21-T800S unidirectional Prepreg, with the thickness of 2.208 mm, and the stack sequence of $[\pm 45/0_2/90/0]_2$.

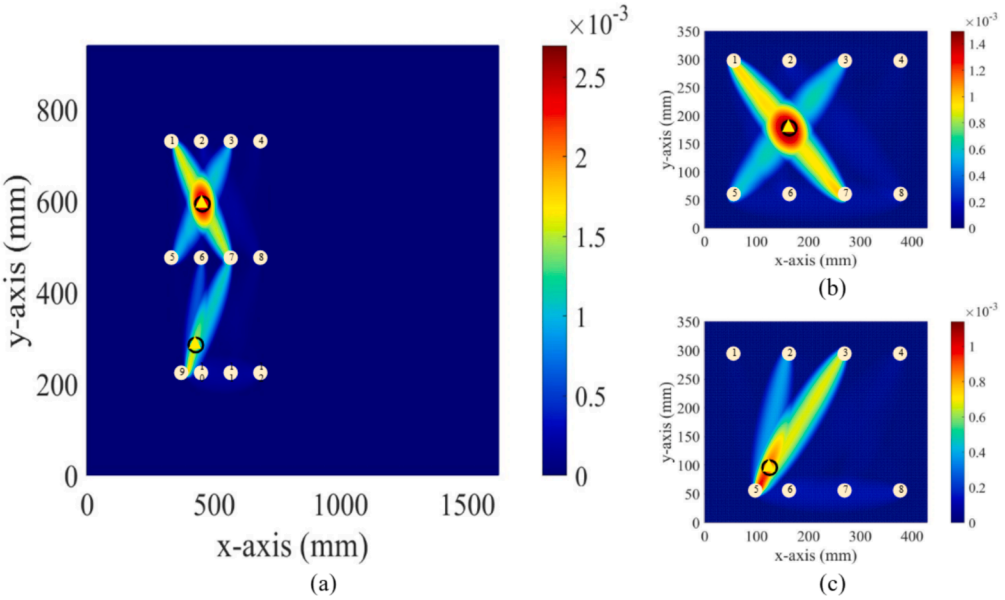


Fig. 15. Damage localization outcome of the dual damage in the stiffened panel. (a) overall localization result, (b) localization result of element 1, (c) localization result of element 2.

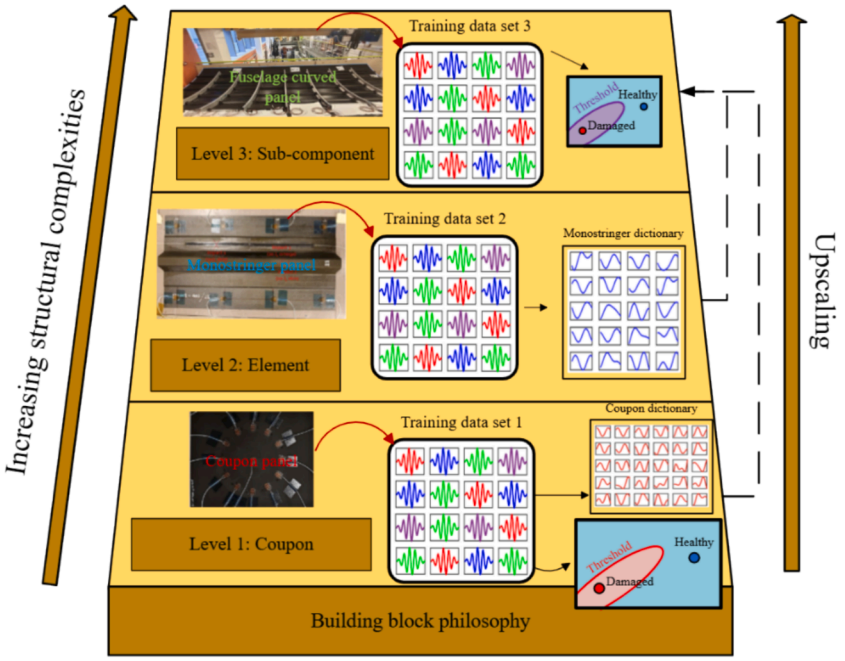


Fig. 16. The information flow of building block (BB) philosophy.

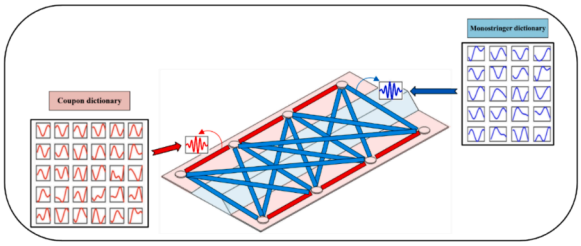


Fig. 17. Illustration of the sparse coding for mono-stringer panels.

To ensure a broad inspection area, a larger network comprised of 72 DuraAct transducers has been installed to the curved fuselage panel, as is depicted in Fig. 18 (b). The sensors are bonded to the panel using a thermoelastic adhesive film, of which the bonding conditions are inspected by the Electro-mechanical Impendence (EMI) [14].

The impact is performed by a PCB Piezotronics Hammer with a custom-made steel tip of 20 mm diameter [14], at Imperial College London.

The linear chirp signal within the range of 10 kHz − 600 kHz is selected as the excitation signal. The acquired guided wave signal data is provided by [14]. The data will then be reconstructed to the 5-cycle Hanning windowed toneburst signal under the central frequency of 50 kHz.

6.3. Element segmentation

As the geometric complexities of higher structural levels increase, Lamb wave propagation is significantly affected by mode conversion and attenuation caused by the presence of mono-stringers and long propagation distances. To address this, it is essential to divide the high-level sub-component into a substantial number of basic elements. Following the sensor selection criteria [48], the curved fuselage panel is segmented into several equivalent elements, each consisting of eight sensors, as shown in Fig. 19 (refer to Appendix C for a complete figure). The sensor paths for each element are illustrated in Fig. 20 (refer to Appendix C for a complete figure). This approach ensures consistent monitoring coverage, facilitating the further implementation of the building block philosophy [40].

For curved panels in Fig. 19, the whole panel can be divided into several sections with 16 sensors. Each 16 sensor-network section is comprised of 3 individual groups with 8 sensors. Each minimum group unit can be regarded as an element. After all elements being extracted from the subcomponent, similar damage identification methodology is applied to detect the potential damage in each element respectively. The implementation of building block philosophy can finally realize the damage identification in the whole large panel [40].

For the pristine curved panel with no damage, the pristine signal of each extracted element could contribute to the pristine training data set, which is further utilized to compute the detectability threshold for damage detection of curved fuselage panels.

6.4. Detectability threshold

A threshold is necessary to differentiate anomalous data indicative of damage from healthy data representing the pristine state. This damage detection can be accomplished through outlier analysis [49,50], utilizing a pristine training dataset of panels at various levels of structural complexity and under different temperature conditions. In this study, the threshold for the curved fuselage panels is established based on the pristine training dataset discussed in Section 6.3. The threshold is determined at the element level, specifically for a curved mono-stringer equipped with eight bonded sensors, as illustrated in Fig. 21 (refer to Appendix C for a complete figure).

The threshold value is defined using chi-squared distribution for the pristine training data set's MSD in Section 2.3. The degree of the chi-squared distribution is set to be 2, and the critical threshold value for MSD is given as 5.9915. Refer to Section 4.2 for a detailed statistical justification of parameter selection. The trained threshold curve for curved fuselage panels is given in Fig. 22 (a). Besides, the threshold curve at coupon levels is given in Fig. 22 (b) and the overall threshold curves are depicted in Fig. 22 (c). Regarding curved fuselage panels in this section, the threshold curve 1 is selected for damage detection.

6.5. Damage detection and localization

6.5.1. Single impact damage

Fig. 23 illustrates the segments extracted from the curved panel where the two single impacts are performed on the upper and lower sides of the stringer's foot, respectively. The impact is performed by a PCB Piezotronics Hammer with a custom-made steel tip of 20 mm diameter [14], at Imperial College London. As is shown in Fig. 24 (a), both impacts can be detected confidently due to the significant distance to the threshold curve. The localization outcomes are depicted in Fig. 24 (b) and (c). It can be found that both the predicted locations (marked as the black circle) are in excellent agreement with the actual damages (marked as the yellow triangle).

In practical engineering, the effect of noise on the fuselage panel is not negligible. Consequently, an analysis of the method's resistance to noise has been conducted to assess the robustness of the proposed averaging approach. The results, presented in Fig. 25 demonstrate the method's effectiveness in mitigating the influence of noise. The effectiveness of the averaging technique has been validated by comparing the quality of the resulting PDIs, which is illustrated in Fig. 25 (a) and (b). Additionally, the Gaussian noise with SNR levels of 1, 5, 10, and 20 has been introduced to the raw signal to assess the method's noise resistance further systematically. Consequently, when the averaging technique is applied, the proposed method exhibits high robustness against random noise variations up to SNR = 20, as illustrated in Fig. 25 (c), (e), (f), and (g).

6.5.2. Multiple damages

Fig. 26 depicts the segment extracted from the curved panel where the two damages are performed under varying temperature within the range of [25:5:50] °C. The groups of sensors are also illustrated in Fig. 26. The objective of the dual damage detection analysis is to validate the feasibility and robustness of the proposed methodology as well as the generated dictionary with respect to EOC, i.e. temperature variations. The detection outcome based on the outlier analysis is given in Fig. 27. The distance to the threshold curve for damage 1 is much larger than that for damage 2, which means that damage 1 is more significant and severer to be detected than damage 2. This has also been validated in the C-scan results of the two damages in Fig. 26, where the impact aeras of damage 1 is much larger than those of damage 2. Only damage 2 under 50 °C are placed inside the threshold curve, which demonstrates the limit for the proposed methodology is temperature variation of $\Delta T = 25^{\circ}$.

The overall Probability-based Diagnostic Imaging (PDIs) of dual damage scenarios under varying temperature within the range of [25:5:50] °C is given in Fig. 28. Both damages can be localized correctly. The respective localisation outcome is given in Fig. 29 and Fig. 30. For damage 2 in Fig. 30, path 8–10 is not as sensitive to the damage presence as path 5–11, making damage 2 less detectable than damage 1. Basically, based on the identification outcomes above, the proposed methodology and generated dictionary are shown to realize the damage identification on the curved fuselage panel under varying temperature $\Delta T = 25^{\circ}$C.

6.6. Detection performance evaluation

The reliability-based threshold has been effectively integrated into the proposed data-driven, transferrable baseline damage detection framework, allowing for a clear distinction between the pristine and damaged states. In this section, a reliability assessment is conducted to evaluate the detection performance based on the threshold curve for curved fuselage panels.

The data set for the reliability assessment in this study is comprised of 143 pristine data points and 18 damaged data points. All data points are based on the experimental tests of the curved fuselage panel. The pristine signal of each extracted element (as is depicted in Fig. 19) contributes to a pristine data point. The damaged data points are comprised of all damage scenarios mentioned in Section 6.5, and other 4 single damage scenarios on the curved fuselage panel, which have been listed in Table 5 and Fig. 31. The overall detection results compilation is depicted in Fig. 32, where 7 undamaged cases show false positives and only 1 damaged case fails to be detected. Additionally, the RAPID images of selected damage scenarios (along with their C-scan results) and one distinct pristine case are included. Notably, the Delay-and-Sum algorithm is integrated with RAPID to improve the accuracy of localizing impacts D-B2 and B-B1. For the internal skin impact D-B2, the RAPID approach is no longer applicable since the impact is not placed at the intersection of at least two detection paths. In other words, only one single detection path (6–7) covers the impact, making it insufficient for accurate localization using the RAPID method alone. Consequently, DAS is integrated with RAPID to address this limitation. However, the localization accuracy still significantly deteriorates, primarily because the impact severity is too slight to be detected. The impact at the skin-foot interface (B-B1) can be localized accurately due to more sufficient detection paths crossing this impact. However, the adjacent light red and yellow regions observed in the fusion PDI result indicate a potential false alarm. This false alarm is primarily because the impact B-B1 was introduced before the fuselage panel had fully recovered from other previous impacts induced by the hammer. The stringer foot impact C-S4 (under 50 °C) cannot be detected because it's placed inside the threshold and is therefore assumed to be an undamaged state. The high temperature and small impact region are the primary factors contributing to this false negative, even though the impact can be correctly localized. However, the RAPID outcome becomes meaningless, as the presence of damage is not confirmed through MSD-based threshold analysis. For the pristine case located just within the threshold curve, no significant damage is observed in the RAPID image. However, the presence of light-yellow regions may be attributed to environmental noise. Subsequently, the *TPR*, *FAR*, *Accuracy* can be calculated by equations (18) (19) (20):

Table 5
Impacted scenarios tested.

Damage scenarios	Damage category	ID	Impact energy (J)	Impact side	Temperature (°C)
Single damage	Skin inside	D-B2	25	Convex	–
	Skin-Foot interference	B-B1	25	Concave	–
	Stringer's foot	D-S1	35	Convex	–
	Stringer's foot	B-S2	35	Convex	–
	Stringer's foot	C-S1	–	Convex	–
	Stringer's foot	C-S4	–	Convex	–
Multiple damages	Stringer's foot	C-S1 + C-S4	–	Convex	[25:5:50]

$$TPR = \frac{TP}{TP + FN} = 0.951 \tag{18}$$

$$FAR = \frac{FP}{TN + FP} = 0.944 \tag{19}$$

$$Accuracy = \frac{TP + TN}{TP + TN + FP + FN} = 0.95 \tag{20}$$

As the result, the reliability and robustness of the detectability threshold at the sub-component level have been validated since the accuracy of the threshold for curved fuselage panels is demonstrated at 95 %.

7. Conclusion

This work proposes a novel scalable data-driven K-SVD based framework for transferrable baseline damage identification on curved fuselage panels. Based on the shapelets generated at lower and less complex levels (i.e. coupon and element) of the building block (BB), the methodology is upscaled to the more complex geometries. This hierarchical framework is comprised of three main sections: dictionary generation, signal reconstruction and damage identification. For dictionary generation, the shapelet dictionary is generated from the pristine data set using K-SVD algorithm. Then the shift dictionary is obtained via shift invariant algorithm for further sparse coding. The detectability of the generated dictionary is verified based on the pristine training data set at lower coupon levels, and further upscaled to the more complex curved fuselage panels. The sparse coding is then implemented to reconstruct the measured signals. It was demonstrated that damage can be reliably detected at a sub-component level (curved fuselage panel) based on the dictionary and threshold calculated at element level (mono-stringer panel) and coupon level (flat coupon panel). Using the data purely from coupons lowers the detectability range at sub-component, hence demonstrating the importance of the scalability of the method following a building block approach. The gap (reconstruction deviation) between the measured signal and the reconstructed one is used for further damage identification within a temperature range of 25°C to 50°C, and for multiple damage scenarios on the curved fuselage panel. The reliability-based threshold is well integrated into this framework for damage detection. The reliability assessment validates that the pre-defined threshold can distinguish correctly between the damaged states and the healthy states. The accuracy of the threshold for curved fuselage panels was demonstrated at 95 %.

The contributions and innovations of this work are outlined as follows:

Development of a Novel Scalable Data-Driven transferrable baseline Damage Identification Framework: This framework achieves high-accuracy detection outcomes for curved fuselage panels. It further expands upon existing techniques by applying data from coupon (flat composite panels) and element (mono-stringer panels) tests at lower structural levels to curved fuselage panels.

Introduction of the K-SVD Algorithm for Shapelet Learning: The proposed shapelet learning method utilizes the K-SVD algorithm, significantly enhancing processing speed while maintaining strong reconstruction performance for curved fuselage panels.

Integration of a Reliability-Based Threshold: For the first time, this framework incorporates a reliability-based threshold to assess both the presence and severity of damage. This establishes a detectability threshold for a transferrable baseline technique.

In conclusion, the integration of the reliability-based threshold with the proposed scalable, data-driven K-SVD transferrable baseline methodology has established a practical and reliable guided wave-based damage identification system for complex curved fuselage panels under varying temperature conditions. Other potential methods for shapelet learning which may yield the better reconstruction performance.

CRediT authorship contribution statement

Haomiao Fang: Writing – review & editing, Writing – original draft, Visualization, Validation, Software, Resources, Methodology, Investigation, Formal analysis, Data curation, Conceptualization. **Zahra Sharif Khodaei:** Writing – review & editing, Supervision, Resources, Project administration, Methodology, Conceptualization. **Ferri M.H. Aliabadi:** Writing – review & editing, Supervision, Resources, Project administration, Methodology, Conceptualization.

Declaration of competing interest

The authors declare that they have no known competing financial interests or personal relationships that could have appeared to influence the work reported in this paper.

Acknowledgments

The authors would like to acknowledge Dr. Francisco de Sá Rodrigues at Imperial College London, for his contribution in providing the experimental data of curved fuselage panels, which is analysed in this study. Our gratitude also goes to Dr. Hongmin Zhu for his contribution in supporting with the dispersion removal algorithm.

Appendix A

Algorithm 1 Generating Shapelet Candidates
Require: S: training dataset, L: length of shapelets, Col: number of columns
Ensure: sc: shapelet candidates

1: **function** SHAPELETCANDIDATES (S, L, Col)
2: $sc \leftarrow []$ // to store generated shapelet candidates
3: **for** $i \leftarrow 1$ to $Col(S)$ **do**
4: $Temp \leftarrow S(:, i)$
5: **while** TRUE **do**
6: $cnt \leftarrow 0$
7: **for** $i \leftarrow 1$ to $|Temp| - L + 1$ **do** // to build sliding windows
8: $sc(cnt+1) \leftarrow Temp(i : i+L-1)$ // to extract and store generated shapelet candidates
9: $cnt \leftarrow cnt + 1$
10: **end for**
11: **end while**
12: **end for**
13: **return** sc
14: **end function**

Algorithm 2 Learning shapelets using K-SVD
Require: $sc \in R^{L \times K}$: shapelet candidates, L: length of shapelets, K: number of atoms, T_0: sparse level
Ensure: $D \in R^{L \times K}$: shapelet dictionary

1: **function** KSVDSHAPELETS (sc, L, K, T_0)
2: **Initialization:** Set the initial dictionary $D^{(0)} \in R^{L \times K}$ with ℓ_2 normalized columns. Set $J = 1$.
3: $y \leftarrow sc$
4: **while** NOT CONVERGENCE **do**
5: **for** $i \leftarrow 1$ to N **do**
6: $x_i \leftarrow x(:, i)$
7: $y_i \leftarrow y(:, i)$
8: $x_i \leftarrow \mathrm{OMP}(D, y_i, T_0)$ // use OMP to compute the sparse representation $x(:, i)$ for each column of y
9: $x \leftarrow [x_1, x_2, \cdots, x_N]$
10: **end for**
11: **for** $k \leftarrow 1$ to $K \in D^{(J-1)}$ **do** // update each column of D
12: $\omega_k \leftarrow \{i | 1 \le i \le N, x(k, i) \neq 0\}$ // to find the nonzero entries in $x(k, :)$
13: $E_k \leftarrow y - \sum_{j \neq k} D(:, j) x(j, :)$ // compute the relevant error matrix
14: $E_k^R \leftarrow E_k(:, \omega_k)$// shrink the error matrix
15: $x_k^R \leftarrow x(k, \omega_k)$
16: $U, \Delta, V^T \leftarrow \mathrm{SVD}(E_k^R)$ // apply SVD decomposition
17: $d(:, k) \leftarrow U(:, 1)$// update dictionary atom d_k to be the first column of U
18: $x(k, \omega_k) \leftarrow \Delta(1,1) V(:, 1)^T$// update sparse coefficients
19: **end for**
20: **end while**
21: **end function**

.

Algorithm 3: Orthogonal Matching Pursuit (OMP)

function $\mathrm{OMP}(D, y, T_0)$
$r \leftarrow y$ // Initialize residual
$x \leftarrow 0$ // Initialize sparse code
$S \leftarrow \varnothing$ // Initialize support set
for $t \leftarrow 1$ to T_0 **do**
$j \leftarrow argmax_j \left| d_j^T r \right|$ // Select atom with maximum correlation
$S \leftarrow S \cup \{j\}$ // Update support set
$x_s \leftarrow argmin_{x_s} \|y - D_S x_s\|_2^2$ // Solve least squares problem
$r \leftarrow y - D_S x_s$ // Update residual
end for
return x
end function

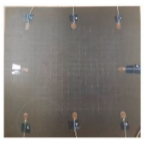
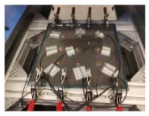
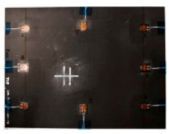
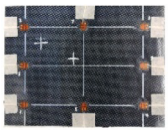
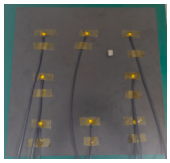
Algorithm 4 Generating Shift-Invariant Dictionary
Require: $D \in R^{L \times K}$: shapelet dictionary, L: length of shapelets, K: number of shapelets, L_2: target length of atoms in the shift-invariant dictionary
Ensure: D_{si}: shift-invariant dictionary

function SHIFTINVARIANTDICTIONARY (D, L, K, L_2)
$D_{si} \leftarrow []$ // to store generated atoms with target length
$cnt \leftarrow 0$
for $i \leftarrow 1$ to K **do**
$T \leftarrow D(:, i)$
for $i \leftarrow 1$ to $L_2 - L + 1$ **do** // to create the atoms with the same shapelets but different time delays, and store them
$A \leftarrow zeros(L_2, 1)$ // Define a $L_2 \times 1$ column vector with all entries initialized to zero
$A(i : i + L - 1) \leftarrow T$
$D_{si}(cnt + 1) \leftarrow A$
$cnt \leftarrow cnt + 1$
end for
end for
return D_{si}
end function

Appendix b

.

Table A2
Pristine data set distribution.

No	Structure items	Dimensions ($mm \times mm$)	Thickness (mm)	Material	Stack sequences	Sensor network size	Temperature conditions (°C)	Total number of signals	
1	Coupon	450 × 450	2	IM7-8552	16	8	[-20:5:50]	15 × 56	
2	Coupon	400 × 400	2.2	T800-M21S	12	9	20	1 × 72	
3	Coupon	300 × 225	2.2	T800-M21S	12	8	[-50:5:70]	25 × 56	
4	Coupon	300 × 225	2.79	PEEK/HTA-40	9	8	[-15:5:45]	11 × 56	
5	Coupon	500 × 500	1.8	T300	9	8	20	1 × 56	

(*continued on next page*)

Table A2 (*continued*)

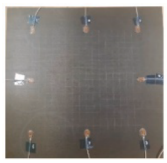
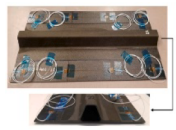
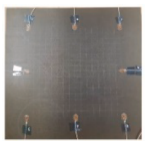
No	Structure items	Dimensions ($mm \times mm$)	Thickness (mm)	Material	Stack sequences	Sensor network size	Temperature conditions (°C)	Total number of signals	
6	Coupon	500 × 500	–	–	–	8	–	1 × 56	
7	Mono-stringer	500 × 250	2.2	T800-M21S	12	8	–	1 × 56	
8	Mono-stringer	500 × 250	2.2	T800-M21S	12	8	[20:5:35]	4 × 56	

Table A4
Training data set distribution.

No	Structure items	Dimensions ($mm \times mm$)	Thickness (mm)	Material	Stack sequences	Sensor network size	Temperature conditions (°C)	Total number of signals	
1	Coupon	450 × 450	2	IM7-8552	16	8	[40:5:45]	2 × 56	
2	Coupon	300 × 225	2.2	T800-M21S	12	8	[-50:5:70]	25 × 56	

Appendix C

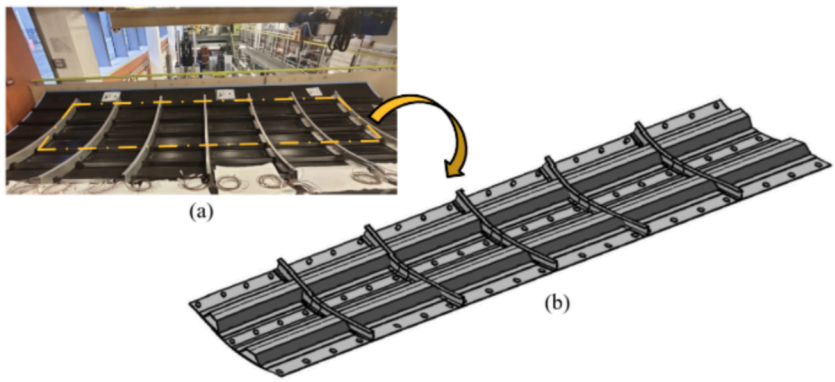


Fig. 18. Illustration of curved aircraft panel in the SHERLOC CleanSky2 project [14].

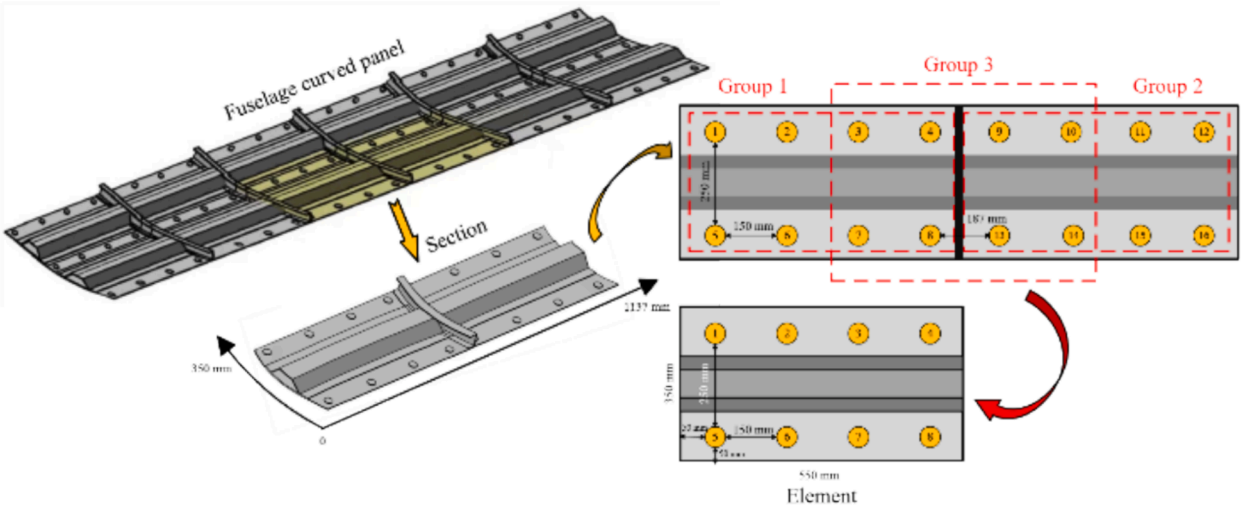


Fig. 19. Illustration of element segmentation from the sub-component structures.

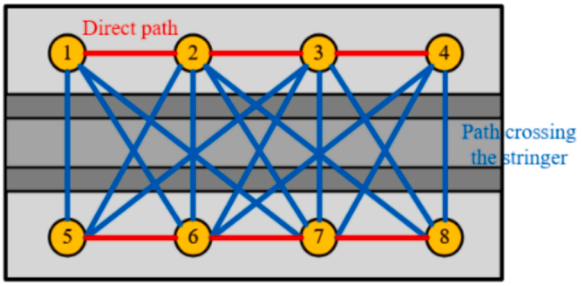


Fig. 20. Illustration of sensor path selection.

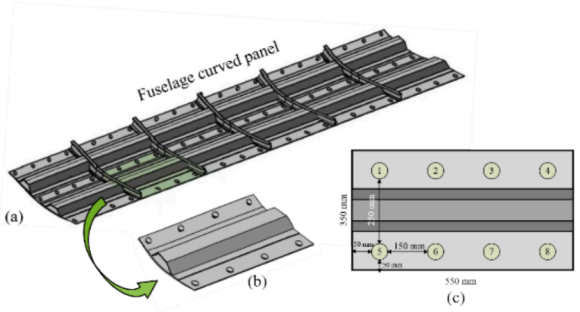


Fig. 21. Illustration of (a) SHERLOC curved panel and (b) (c) element extracted from the sub-component.

Appendix D

Comparison with unsupervised shapelet algorithm

In this section, the unsupervised shapelet (u-shapelet) algorithm [33] has been applied to generate u-shapelet coupon dictionary. Refer to [33] for the detailed fundamentals of u-shapelet algorithm. Taking coupons as the example, the generated dictionary is shown in Fig. 34. Fig. 33 depicts the M21-T800S coupon panel with the dimension of 400mm × 400mm × 2*mm* and the stacking layer sequence of $[\pm 45/0_2/90/0]_2$. 12 DuraAct sensors are mounted in the circular distribution with the radius of 140 mm. The added mass is introduced to simulate the skin damages at 5 different locations [19].

The theoretical analysis of computational complexity reveals that K-SVD and unsupervised shapelet algorithms exhibit distinct scalability characteristics. The K-SVD algorithm involves two main computational steps: sparse coding and dictionary update. The sparse coding step, often solved using Orthogonal Matching Pursuit (OMP) or LASSO, has a complexity defined as $O(NKL)$, where N, K, L represents the number of shapelet candidates (training samples), number of atoms in the dictionary, and length of shaplets, respectively. While the dictionary update step, which involves Singular Value Decomposition (SVD), scales as $O(K^2L)$. The overall

complexity per iteration is therefore $O(NKL + K^2L)$, making K-SVD computationally efficient for large datasets when K remains relatively small.

In contrast, unsupervised shapelet algorithms, which identify discriminative subsequences in time series, typically require an exhaustive search over all possible shapelets, resulting in significantly higher computational costs. A brute-force approach incurs a complexity of $O(N^2L^4)$, where N is the number of time series (equal to the number of shapelet candidates in K-SVD) and L is the sequence length (equal to the length of shapelets in K-SVD), making it infeasible for large-scale applications. Consequently, K-SVD generally exhibits superior computational efficiency, particularly for large datasets, whereas shapelet-based methods require substantial optimization to be practically viable.

Additionally, the processing speed of the two algorithms and the performance of their respective dictionaries have been compared and evaluated empirically, as is given in Table 6, Fig. 35 and Fig. 36. In Fig. 35, the black circle and white triangle represent predicted and actual damage, respectively. The performance is evaluated based on the detection results of five damage scenarios. The accuracy of detection results is defined by equation (21):

$$Accuracy = \sqrt{(x - x_{true})^2 + (y - y_{true})^2} \tag{21}$$

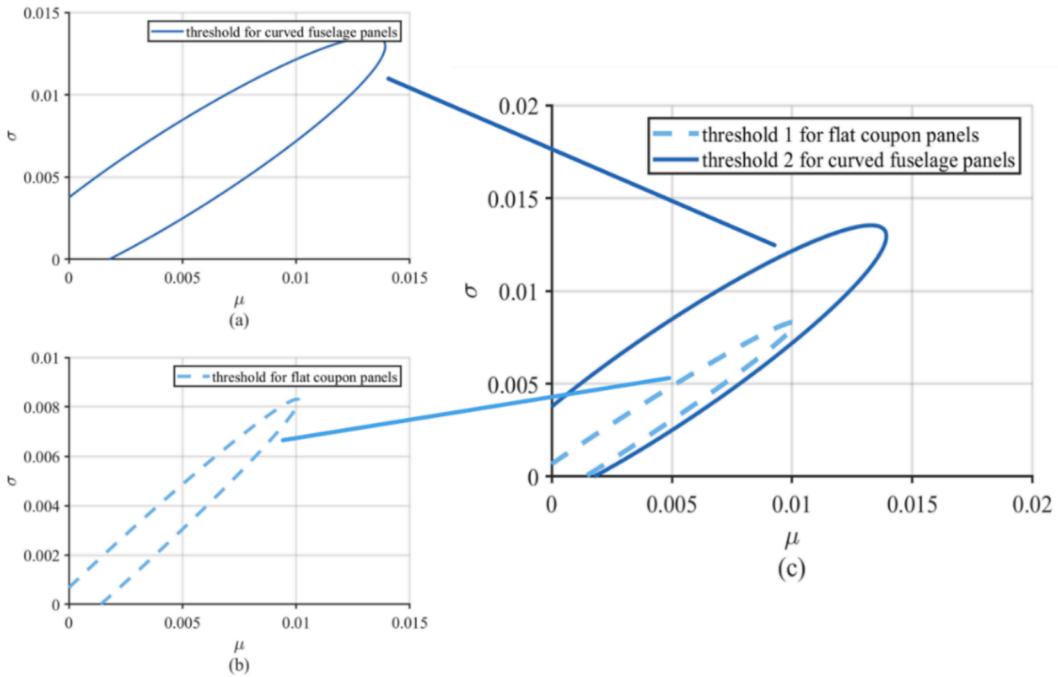


Fig. 33. A coupon for the case of 5 single damages.

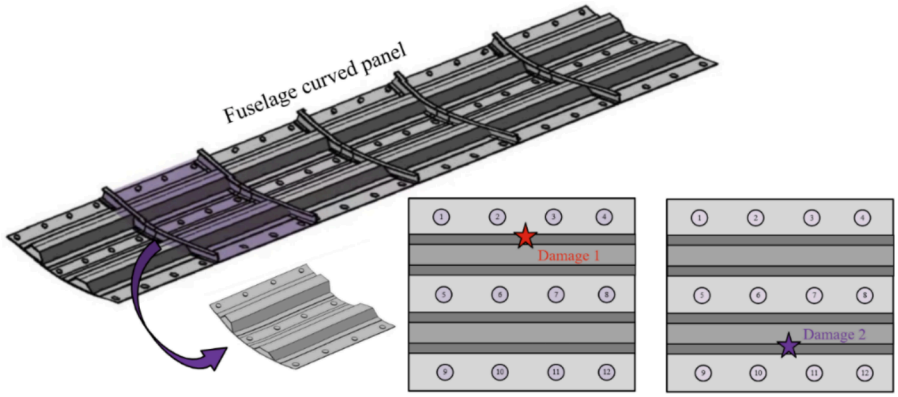


Fig. 34. Coupon dictionary based on u-shapelet algorithm.

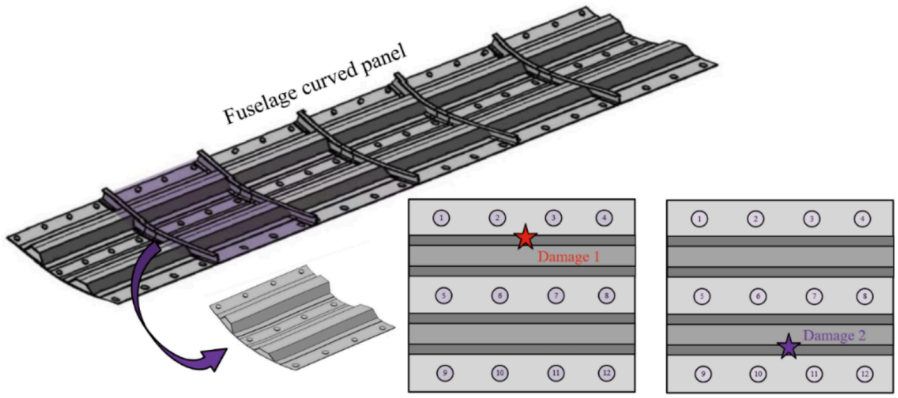


Fig. 35. Damage localization results using the generated dictionary based on (a) (b) (c) (d) (e) u-shapelet and (f) (g) (h) (i) (j) K-SVD algorithm.

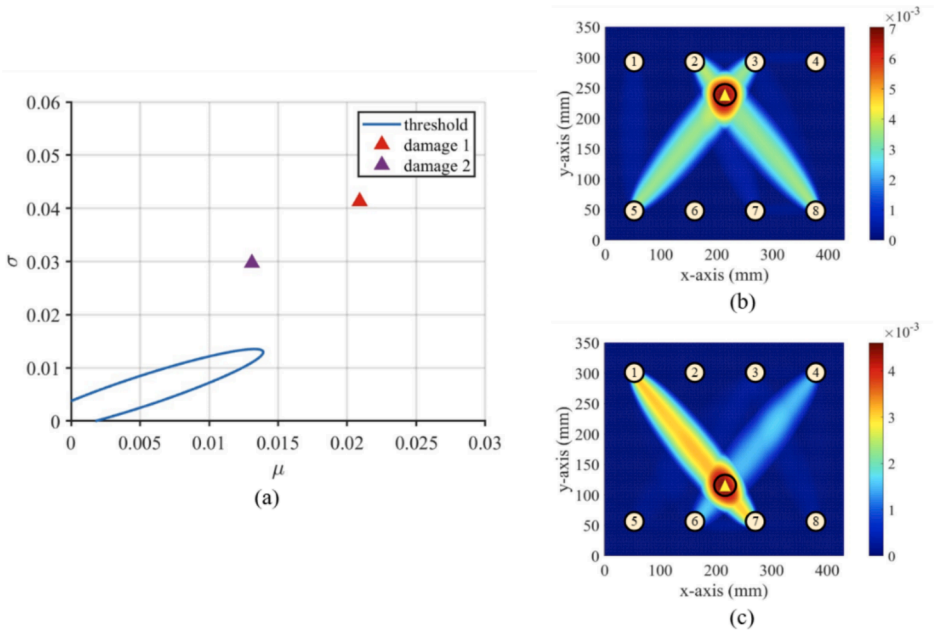


Fig. 36. Comparison of the computational time of the two algorithms.

Table 6
Comparison of the processing speed and accuracy among the two algorithms.

	Number of candidates	Iterations	Time (s)	Performance (accuracy) (mm)
U-shapelet algorithm	1820	–	279	10.44/8.00/7.07/5.00/5.83
	3640	–	385	10.44/8.00/7.07/5.00/5.83
	4680	–	491	10.44/8.00/7.07/5.00/5.83
	10,140	–	1306	10.44/8.00/7.07/5.00/5.83
K-SVD algorithm	1820	200	5	10.44/8.00/7.07/5.00/5.83
		500	11	10.44/8.00/7.07/5.00/5.83
		1000	25	10.44/8.00/7.07/5.00/5.83
	3640	200	7	10.44/8.00/7.07/5.00/5.83
		500	16	10.44/8.00/7.07/5.00/5.83
		1000	34	10.44/8.00/7.07/5.00/5.83
	4680	200	15	10.44/8.00/7.07/5.00/5.83
		500	32	10.44/8.00/7.07/5.00/5.83
		1000	63	10.44/8.00/7.07/5.00/5.83
	10,140	200	31	10.44/8.00/7.07/5.00/5.83
		500	77	10.44/8.00/7.07/5.00/5.83
		1000	156	10.44/8.00/7.07/5.00/5.83

As is shown, the accuracy of both algorithms is similar for flat coupon panels. However, the u-shapelet algorithm is much more time-consuming than K-SVD algorithm. Especially for the large data set, the original u-shapelet algorithm is computationally expensive. Here in this problem, the number of the shapelet candidates (197,600) is significantly large, which cannot be solved by the u-shapelet algorithm.

Another limitation of the u-shapelet algorithm is that it is not as flexible as K-SVD. In the u-shapelet algorithm, only the parameter k (total number of clusters) can be adjusted to indirectly control the number of the shapelets. That means we cannot obtain every number of the shapelets as expected. But for K-SVD, the number of the shapelets can be directly controlled.

Additionally, a decreased detection capability and the large detection error have been found in the more complex stiffened panels using the u-shapelet dictionary [32]. This constraint will be solved based on the proposed K-SVD based methodology in the following sections.

Appendix e

In this study, we address these challenges by integrating the delay-and-sum (DAS) algorithm with RAPID in K-SVD transferrable baseline method to enhance both spatial and temporal resolution in damage imaging. The virtual baseline for the entire test signal is reconstructed using pre-trained shapelets, with its length adjusted to 300. The delay-and-sum imaging is obtained using equation (22):

$$I_{DAS}(x,y) = \frac{1}{n}\sum_{j=1}^{n} \mathscr{H}\left(\mathscr{B}_j(t) - \mathbb{C}_j(t)\right) \tag{22}$$

Where the operator $\mathscr{H}(\bullet)$ is Hilbert transform, $\mathscr{B}_j(t) - \mathbb{C}_j(t)$ represents the residual between the virtual baseline and the test signal for sensor pair j. Consequently, the fusion image can be expressed as:

$$I_{Fusion}(x,y) = I_{DAS}(x,y) * I_{RAPID}(x,y) \tag{23}$$

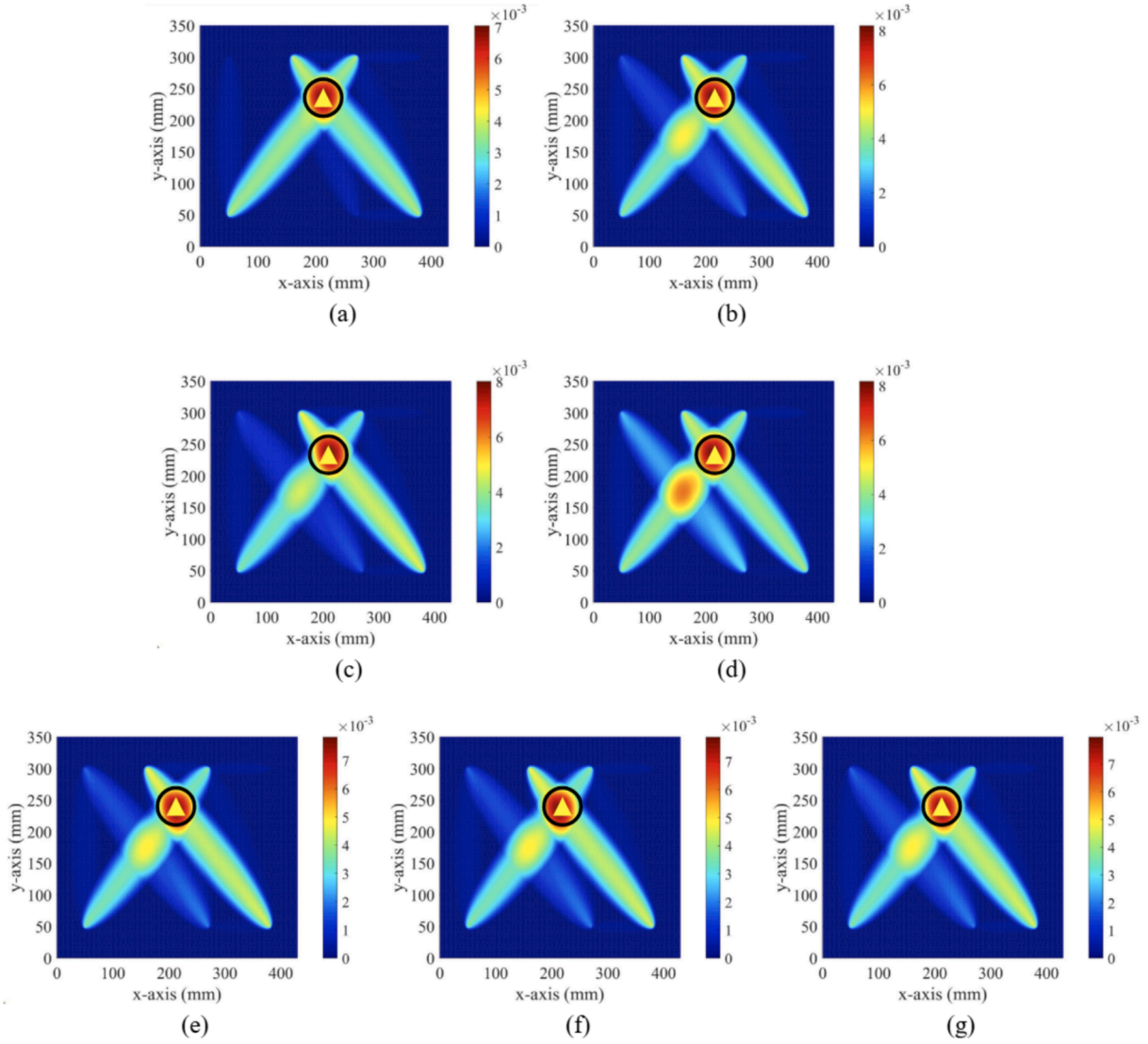


Fig. 37. The refined fusion PDI localization result.

Taking the impact at 20 °C as an example, the refined fusion image is shown in Fig. 37, with the black circle indicating the predicted damage and the yellow triangle indicating the actual one. Consequently, the fusion localization result demonstrates a reduced discrepancy between the predicted and actual damage locations. Additionally, the adjacent noise—represented by the yellow region near the predicted damage, has been significantly suppressed.

Appendix F

All damage detection and localization studies in this paper based on the dictionary trained from pristine signals at 25 °C are supplemented here for a systematic side-by-side comparison with those trained under varying temperatures. Although the damage state vectors differ from those based on the dictionary trained at 25 °C in MSD-based damage detection, all but one damage scenario fall outside the threshold and are effectively detected. The results show a good alignment with the previous dictionary trained under varying temperatures. Comparably, the detection and localization outcomes match quite similarly despite the minor differences in

damage indexes. That is because the post-processing techniques (Section 2.1) are applied to these signals in the very beginning, effectively removing their original temperature-dependent information. Detailly, the first wavepacket extraction and normalization (which rescales the signal amplitude within [-1,1]) techniques are implemented to mitigate phase and amplitude variations induced by temperature changes. Consequently, the influence of EOCs on the training set is significantly reduced, enhancing the robustness of the proposed framework to temperature variations.

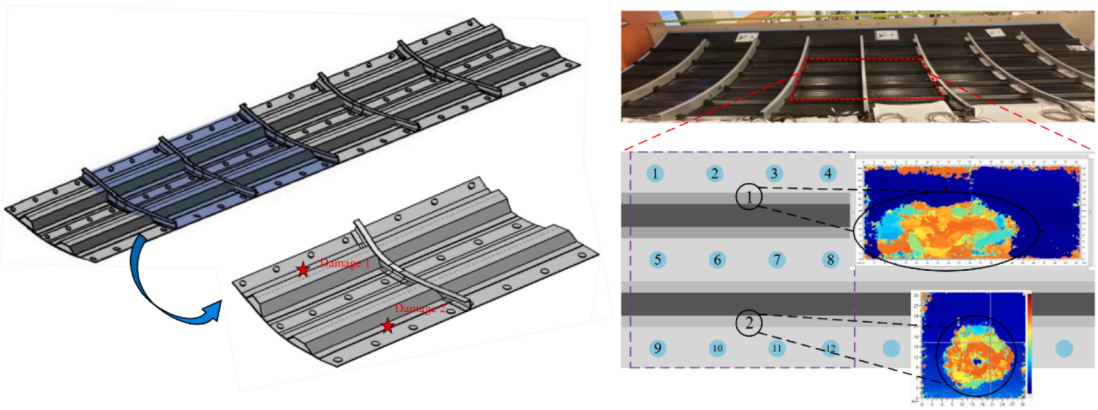


Fig. 38. Damage detection results using the dictionary trained from pristine signals purely at 25 °C.

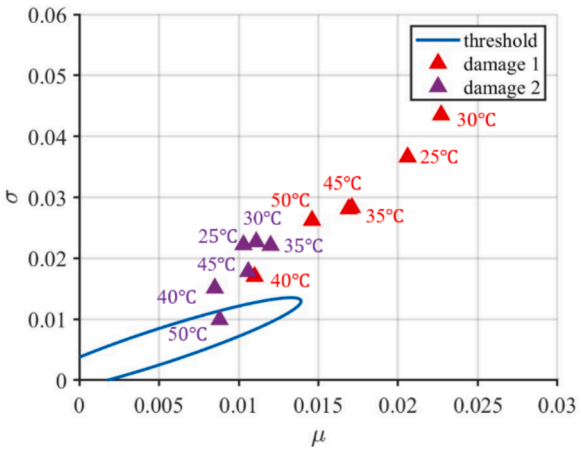


Fig. 39. Damage localization results using the dictionary trained from pristine signals purely at 25 °C.

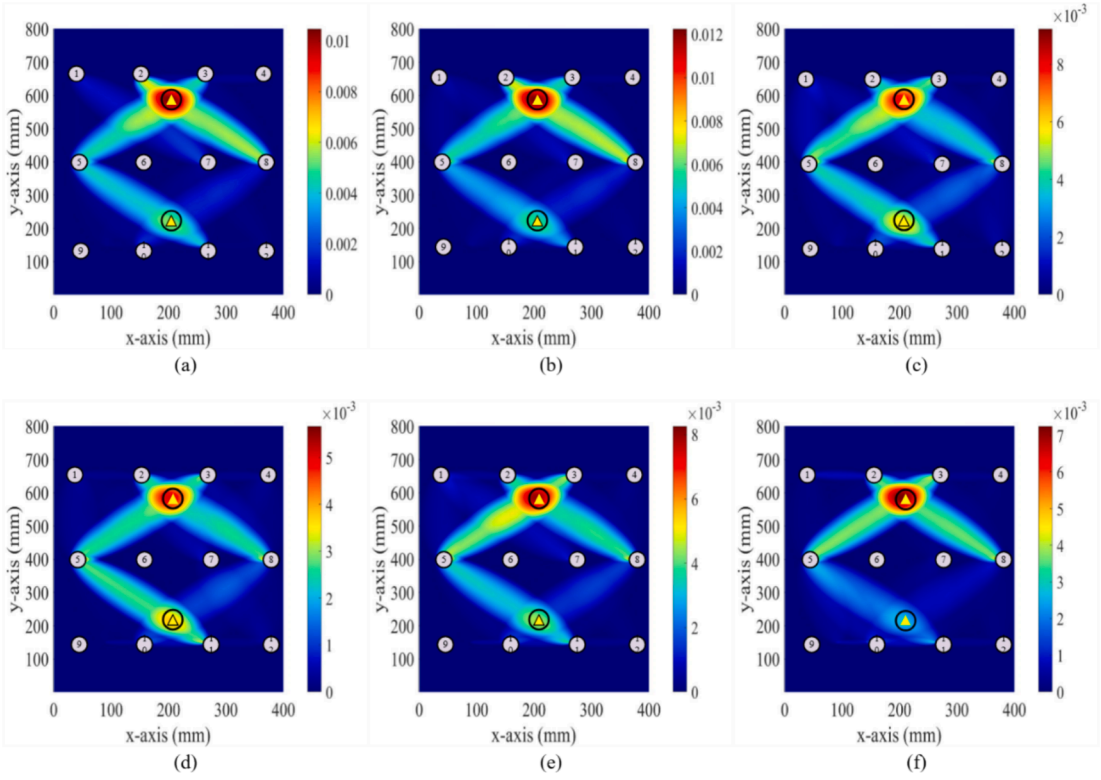


Fig. 40. Damage detection outcome of the impacts under varying temperature using the dictionary trained from pristine signals purely at 25 °C.

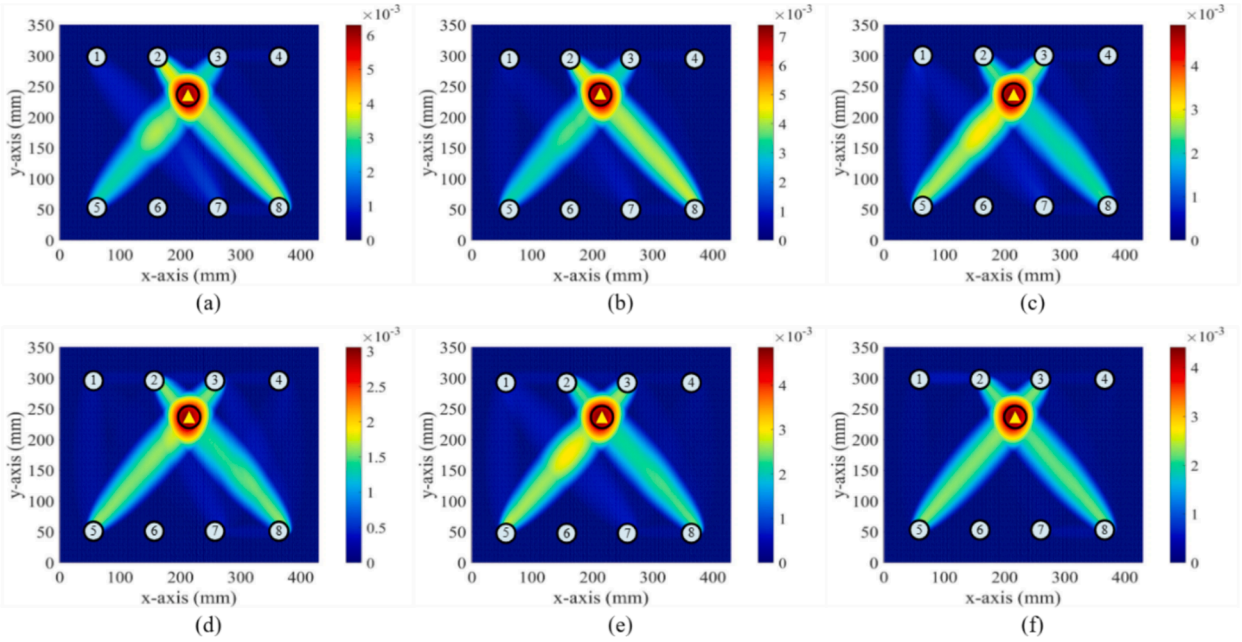


Fig. 41. Damage localization outcome of the impacts at (a) 20 °C, (b) 25 °C, (c) 30 °C, (d) 35 °C, (e) 40 °C, (f) 45 °C using the dictionary trained from pristine signals purely at 25 °C.

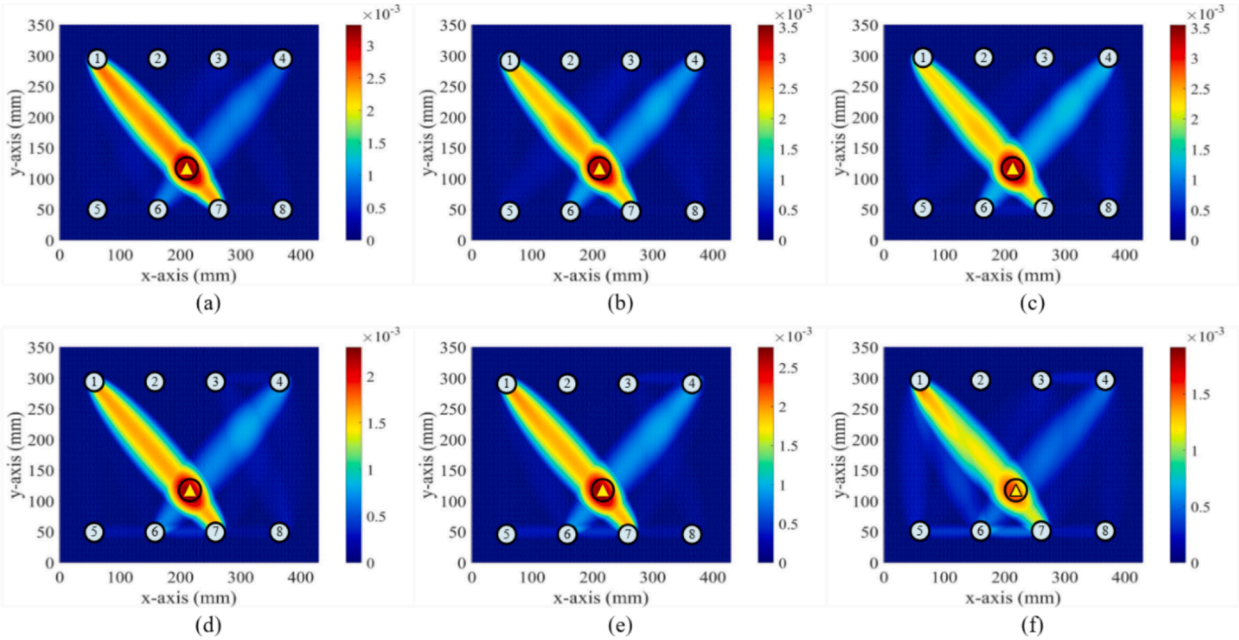


Fig. 42. Damage detection outcome of the dual damage in the stiffened panel using the dictionary trained from pristine signals purely at 25 °C.

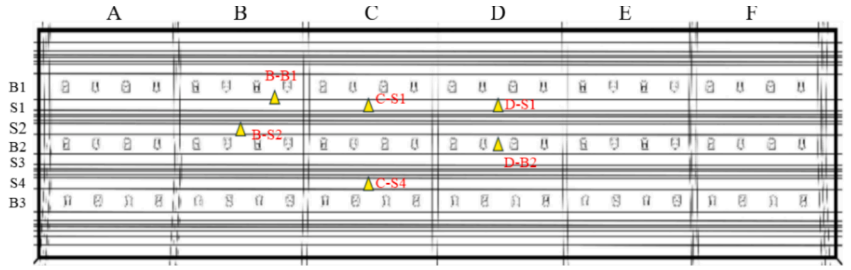


Fig. 43. Damage localization outcome of the dual damage in the stiffened panel using the dictionary trained from pristine signals purely at 25 °C。

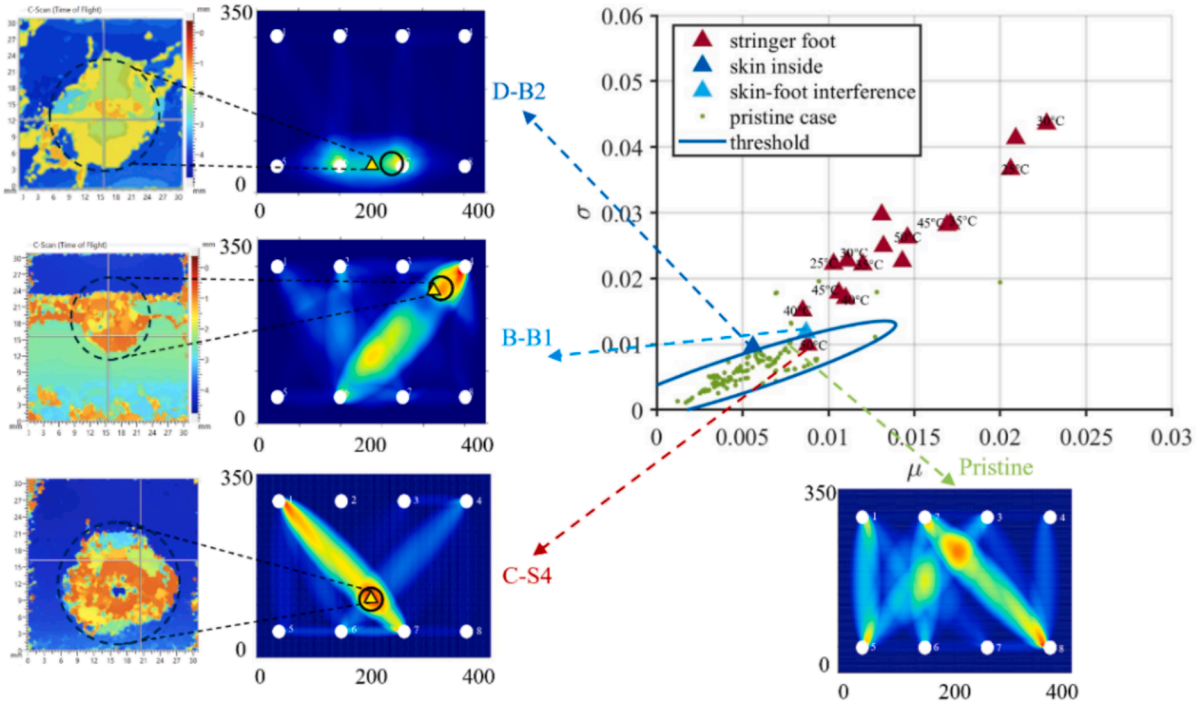


Fig. 44. Damage (a) detection and (b) (c) localization outcomes of the two single damages using the dictionary trained from pristine signals purely at 25 °C.

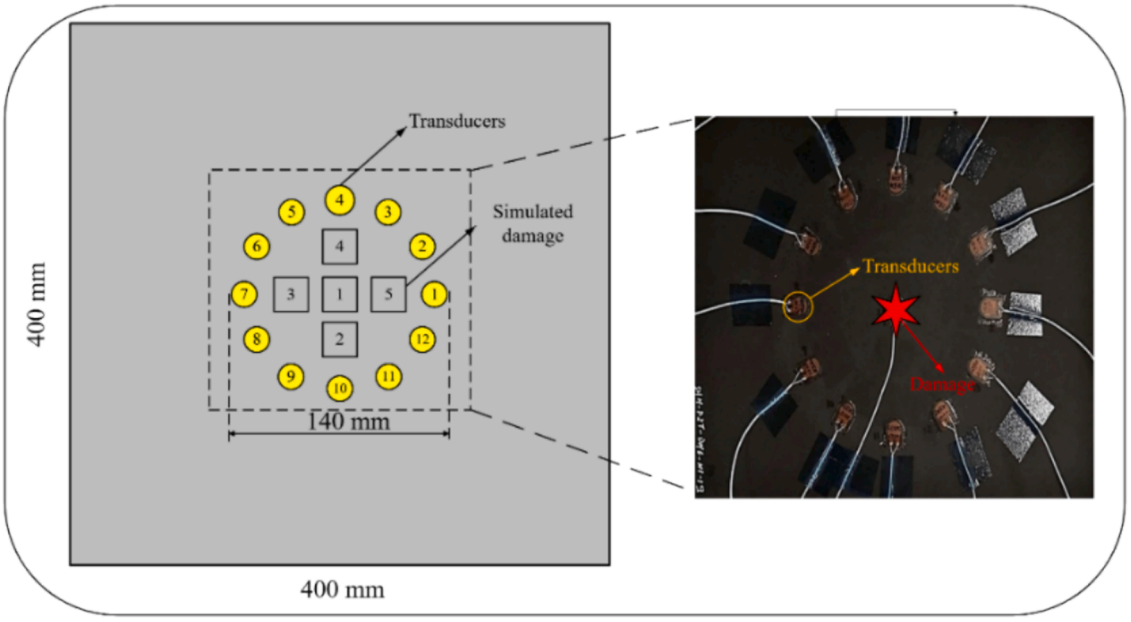


Fig. 45. Damage localization outcome of the dual damage under varying temperature using the dictionary trained from pristine signals purely at 25 °C.

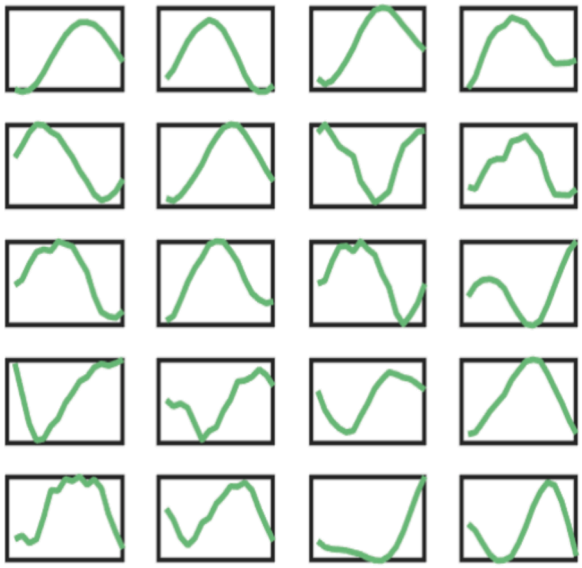


Fig. 46. Damage localization outcome for element 1 of the dual damage at (a) 25 °C, (b) 30 °C, (c) 35 °C, (d) 40 °C, (e) 45 °C, (f) 50 °C in the curved aircraft panel using the dictionary trained from pristine signals purely at 25 °C.

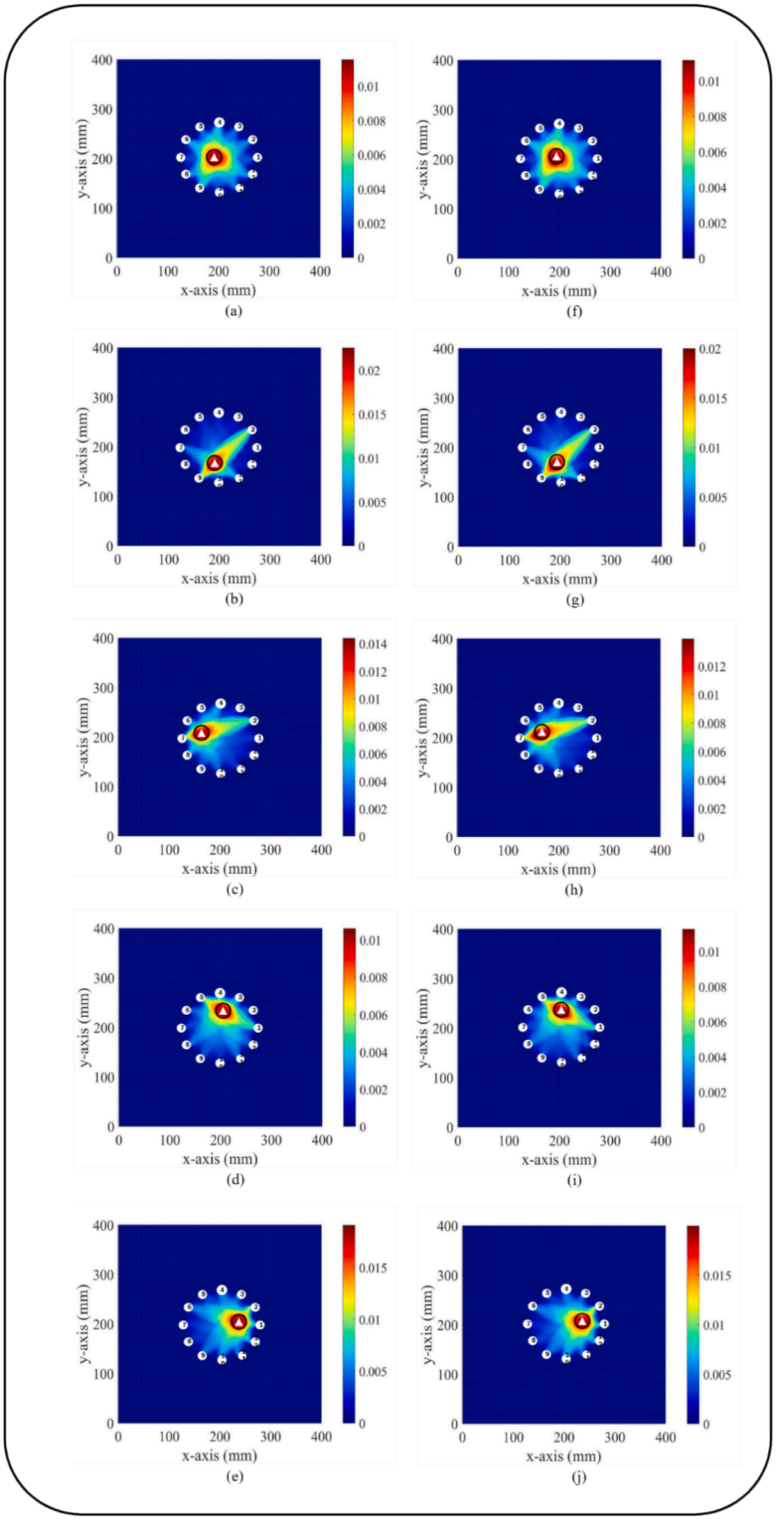


Fig. 47. Damage localization outcome for element 2 of the dual damage at (a) 25 °C, (b) 30 °C, (c) 35 °C, (d) 40 °C, (e) 45 °C, (f) 50 °C in the curved aircraft panel using the dictionary trained from pristine signals purely at 25 °C.

Data availability

Part of data will be made available on request. Fuselage data remains confidential and will be released in the future.

References

[1] Kumar, D., Kalra, S., and Jha, M.S.: 'Recent Advancements on Structural Health Monitoring Using Lamb Waves', in Editor (Ed.)^(Eds.): 'Book Recent Advancements on Structural Health Monitoring Using Lamb Waves' (Springer Singapore, 2022, edn.), pp. 131-142.
[2] Z. Yang, H. Yang, T. Tian, D. Deng, M. Hu, J. Ma, D. Gao, J. Zhang, S. Ma, L. Yang, H. Xu, Z. Wu, A review on guided-ultrasonic-wave-based structural health monitoring: From fundamental theory to machine learning techniques, Ultrasonics 133 (2023) 107014.
[3] C.L. Wilson, K. Lonkar, S. Roy, F. Kopsaftopoulos, F.-K. Chang, in: 7.20 Structural Health Monitoring of Composites, (Elsevier, 'Comprehensive Composite Materials II', 2018, pp. 382–407.
[4] Aliabadi, M.H.F., and Khodaei, Z.S.: 'Structural Health Monitoring for Advanced Composite Structures', in Editor (Ed.)^(Eds.): 'Book Structural Health Monitoring for Advanced Composite Structures' (2018, edn.), pp.
[5] Verma, R., and Shukla, A.: 'Structural Health Monitoring of Aerospace Composites' (2018), pp. 33-52.
[6] Ross, R.W.: '1 - Integrated vehicle health management in aerospace structures', in Yuan, F.-G. (Ed.): 'Structural Health Monitoring (SHM) in Aerospace Structures' (Woodhead Publishing, 2016), pp. 3-31.
[7] Derriso, M.M., McCurry, C.D., and Schubert Kabban, C.M.: '2 - A novel approach for implementing structural health monitoring systems for aerospace structures', in Yuan, F.-G. (Ed.): 'Structural Health Monitoring (SHM) in Aerospace Structures' (Woodhead Publishing, 2016), pp. 33-56.
[8] M. Mitra, S. Gopalakrishnan, Guided wave based structural health monitoring: A review, Smart Mater. Struct. 25, (5) (2016) 053001.
[9] P.D. Wilcox, G. Konstantinidis, A.J. Croxford, B.W. Drinkwater, Strategies for Guided Wave Structural Health Monitoring, AIP Conf. Proc. 894 (1) (2007) 1469–1476.
[10] F. Yan, R.L. Royer, J.L. Rose, 'Ultrasonic Guided Wave Imaging Techniques in Structural Health, Monitoring' 21 (3) (2010) 377–384.
[11] M. Philibert, K. Yao, M. Gresil, C. Soutis, Lamb waves-based technologies for structural health monitoring of composite structures for aircraft applications, European Journal of Materials 2 (1) (2022) 436–474.
[12] X. Zhao, H. Gao, G. Zhang, B. Ayhan, F. Yan, C. Kwan, J.L. Rose, Active health monitoring of an aircraft wing with embedded piezoelectric sensor/actuator network: I. Defect detection, localization and growth monitoring, Smart Mater. Struct. 16, (4) (2007) 1208.
[13] L. Li, P. Fromme, Mode conversion of fundamental guided ultrasonic wave modes at part-thickness crack-like defects, Ultrasonics 142 (2024) 107399.
[14] F. de Sá Rodrigues, I.N. Giannakeas, Z. Sharif Khodaei, F.M.H. Aliabadi, Probability based damage detection on a composite fuselage panel based on large data set of guided wave signals, NDT and E Int. 139 (2023) 102924.
[15] F. Ren, I. Giannakeas, Z. Khodaei, M. Aliabadi, Theoretical and experimental investigation of guided wave temperature compensation for composite structures with different thicknesses, Mech. Syst. Sig. Process. 200 (2023) 110594.
[16] M. Kannusamy, S. Kapuria, S. Sasmal, An efficient Lamb wave-based virtual refined time-reversal method for damage localization in plates using broadband measurements, Ultrasonics 124 (2022) 106767.
[17] H.W. Park, S.B. Kim, H. Sohn, Understanding a time reversal process in Lamb wave propagation, Wave Motion 46 (7) (2009) 451–467.
[18] F. Du, L. Zeng, L. Huang, J. Rao, A refined Lamb wave reciprocity-based method with enhanced sensitivity for damage detection in composite laminates, Ultrasonics 132 (2023) 106980.
[19] H. Zhu, Z. Sharif Khodaei, M.H. Aliabadi, Investigation of Baseline-free Techniques for Damage Localisation on Anisotropic Composite Structures, Procedia Struct. Integrity 52 (2024) 679–689.
[20] M. Scalerandi, C.L.E. Bruno, A.S. Gliozzi, P.G. Bocca, Break of reciprocity principle due to localized nonlinearities in concrete, Ultrasonics 52 (6) (2012) 712–719.
[21] J. Wang, Y. Shen, An enhanced Lamb wave virtual time reversal technique for damage detection with transducer transfer function compensation, Smart Mater. Struct. 28, (8) (2019) 085017.
[22] Tabatabaeipour, M., Hettler, J., Delrue, S., and Van Den Abeele, K.: 'Reconstruction Algorithm for Probabilistic Inspection of Damage (RAPID) in Composites' (2014. 2014).
[23] V. Nerlikar, R. Miorelli, A. Recoquillay, O. d'Almeida, A physics-embedded deep-learning framework for efficient multi-fidelity modeling applied to guided wave based structural health monitoring, Ultrasonics 141 (2024) 107325.
[24] Fisher, C., Billon, F., Thomas, A., and Druet, T.: 'Deep Learning Method Based on Denoising Autoencoders for Temperature Selection of Guided Waves Signals' (2024. 2024).
[25] O. Mesnil, A. Recoquillay, C. Fisher, V. Serey, S. Sharma, O. d'Almeida, Self-referenced robust guided wave based defect detection: Application to woven composite parts of complex shape, Mech. Syst. Sig. Process. 188 (2023) 109948.
[26] X.L. Tu, R.J. Pyle, A.J. Croxford, P.D. Wilcox, Potential and limitations of NARX for defect detection in guided wave signals, Struct. Health Monit. 22 (3) (2022) 1863–1875, https://doi.org/10.1177/14759217221113240.
[27] S. Ahmed, F. Kopsaftopoulos, 'active Sensing Ultrasonic Guided Wave-Based Damage Diagnosis via Stochastic Stationary Time-Series Models' 23 (4) (2024) 2559–2595.
[28] V. Nerlikar, O. Mesnil, R. Miorelli, O. D'Almeida, 'damage Detection with Ultrasonic Guided Waves Using Machine Learning and Aggregated Baselines' 23 (1) (2024) 443–462.
[29] M. Aharon, M. Elad, A. Bruckstein, K-SVD: An algorithm for designing overcomplete dictionaries for sparse representation, IEEE Trans. Signal Process. 54 (11) (2006) 4311–4322.
[30] A.M. Nokhbatolfoghahai, H. Navazi, R.M. Groves, Use of dictionary learning for damage localization in complex structures, Mech. Syst. Sig. Process. 180 (2022) 109394.
[31] K.S. Alguri, J. Melville, J.B. Harley, Baseline-free guided wave damage detection with surrogate data and dictionary learning, J. Acoust. Soc. Am. 143, (6) (2018) 3807.
[32] H. Zhu, Z.S. Khodaei, F.M.H. Aliabadi, Baseline-free damage detection and localization on complex composite structures using unsupervised shapelets and shift-invariant dictionary learning, Mech. Syst. Sig. Process. 224 (2025) 112035.
[33] Zakaria, J., Mueen, A., and Keogh, E.: 'Clustering Time Series Using Unsupervised-Shapelets', in Editor (Ed.)^(Eds.): 'Book Clustering Time Series Using Unsupervised-Shapelets' (2012, edn.), pp. 785-794.
[34] F. Ren, I.N. Giannakeas, Z. Sharif Khodaei, M.H.F. Aliabadi, The temperature effects on embedded PZT signals in structural health monitoring for composite structures with different thicknesses, NDT and E Int. 141 (2024) 102988.
[35] L. Liu, F.G. Yuan, A Linear Mapping Technique for Dispersion Removal of Lamb Waves, Struct. Health Monit. 9 (1) (2009) 75–86.
[36] B. Xu, L. Yu, V. Giurgiutiu, Lamb wave dispersion compensation in piezoelectric wafer active sensor phased-array applications, Proc. SPIE-Int. Soc. Opt. Eng. (2009).
[37] Ye, L., and Keogh, E.J.: 'Time series shapelets: a new primitive for data mining', in Editor (Ed.)^(Eds.): 'Book Time series shapelets: a new primitive for data mining' (2009, edn.), pp.
[38] Ulanova, L., Begum, N., and Keogh, E.J.: 'Scalable Clustering of Time Series with U-Shapelets', in Editor (Ed.)^(Eds.): 'Book Scalable Clustering of Time Series with U-Shapelets' (2015, edn.), pp.
[39] Mairal, J., Bach, F., Ponce, J., and Sapiro, G.: 'Online dictionary learning for sparse coding' (2009. 2009).

[40] N. Yue, Z. Sharif Khodaei, M.H. Aliabadi, Damage detection in large composite stiffened panels based on a novel SHM building block philosophy, Smart Mater. Struct. 30 (2021).
[41] R. Domingues, M. Filippone, P. Michiardi, J. Zouaoui, A comparative evaluation of outlier detection algorithms: Experiments and analyses, Pattern Recogn. 74 (2018) 406–421.
[42] Mahalanobis, P.C.: 'On the generalized distance in statistics', in Editor (Ed.)'(Eds.): 'Book On the generalized distance in statistics' (1936, edn.), pp.
[43] N. Yue, M.H. Aliabadi, Hierarchical approach for uncertainty quantification and reliability assessment of guided wave-based structural health monitoring, Struct. Health Monit. 20 (5) (2020) 2274–2299.
[44] J. Hettler, M. Tabatabateipour, S. Delrue, K. Van Den Abeele, Application of a Probabilistic Algorithm for Ultrasonic Guided Wave Imaging of Carbon Composites, Phys. Procedia 70 (2015) 664–667.
[45] R. Rubinstein, M. Zibulevsky, M. Elad, Efficient Implementation of the K-SVD Algorithm Using Batch Orthogonal Matching Pursuit, CS Technion 40 (2008).
[46] N. Yue, Z. Sharif Khodaei, M.J.K.E.M. Aliabadi, 'an Innovative Secondary Bonding of Sensors to Composite Structures for SHM Application' 774 (2018) 516–522.
[47] G. Galanopoulos, E. Fytsilis, N. Yue, A. Broer, D. Milanoski, D. Zarouchas, T. Loutas, A data driven methodology for upscaling remaining useful life predictions: From single- to multi-stiffened composite panels, Composites, Part C: Open Access 11 (2023) 100366.
[48] I.N. Giannakeas, Z. Sharif Khodaei, M.H. Aliabadi, An up-scaling temperature compensation framework for guided wave–based structural health monitoring in large composite structures, Struct. Health Monit. 22 (2) (2022) 777–798.
[49] K. Worden, G. Manson, N.R.J. Fieller, DAMAGE DETECTION USING OUTLIER ANALYSIS, J. Sound Vib. 229 (3) (2000) 647–667.
[50] K. Worden, S.G. Pierce, G. Manson, W.R. Philp, W.J. Staszewski, B. Culshaw, Detection of defects in composite plates using Lamb waves and novelty detection, Int. J. Syst. Sci. 31 (11) (2000) 1397–1409.